Attempt to Control the Anisotropy of Topological Surface States

R. Yamamoto[a], K. Sumida[b], K. Miyamoto[b], and T. Okuda[b].

[a]*Graduate School of Advanced Science and Engineering Hiroshima University, 1-3-1 Kagamiyama Higashi-Hiroshima 739-8526, Japan*
[b]*Hiroshima Synchrotron Radiation Center (HSRC), Hiroshima University 2-313 Kagamiyama, Higashi-Hiroshima 739-0046, Japan*

Keywords: Topological Surface States, Silicon Vicinal Surface, Anisotropy of Band Structure, Bi_2Te_3 film

Topological insulators have spin-polarized conduction states on their surfaces (= topological surface states), where the spin direction of electrons is locked by their momentum resulting the helical spin-texture. The unique helical spin-texture is considered to prohibit complete backscattering by non-magnetic impurities. Thus, the surface of topological insulators is expected to be promising platform for spintronics devices. However, other backscattering passes except for the complete backscattering are not prohibited [Fig.1(a)]. One solution to suppress the backscattering is forming an anisotropic Fermi surface, ideally a one-dimensional Fermi surface[Figs. 1(b) and 1(c)].

In previous research, it has been reported that Ag films on Si(111)-(4×1)-In, which has an array of In chains, exhibit a quasi-one-dimensional band structure [1]. This result is attributed to the confinement of electrons in the quasi-one-dimensional Ag films caused by the step and terrace structure, and a similar effect can be expected even on vicinal surface. The vicinal silicon surface has atomically regular step arrays and electron motion in the film grown on the surface might be restricted only one direction parallel to the step. From this analogy, we considered that it might be possible to obtain the anisotropic spin-polarized band structure by growing Bi_2Te_3 films on silicon vicinal surface. However, there is no report of the fabrication of Bi_2Te_3 film on silicon vicinal surface so far. Therefore, the purposes of this research are to fabricate Bi_2Te_3 film on silicon vicinal surface, measure the band structure, and evaluate the band anisotropy.

In our study, we grew Bi_2Te_3 ultrathin films on Si(111) and Si(557) by molecular beam epitaxy, which were used as flat and vicinal surface substrate, respectively. Si(557) is a surface tilted by 9.5° from Si(111), and its terraces have the same plane as Si(111). We checked the quality of surface structure by low energy electron diffraction (LEED) and auger electron spectroscopy (AES). Figure 2 shows LEED patterns and the spectra of AES of Bi_2Te_3 film on each substrate. As in Fig. 2, we can see clear spots in LEED and peak of Bi and Te in AES indicating that we could succeed to grow Bi_2Te_3 film on vicinal silicon surface.

To observe the band structure of the fabricated films, angle-resolved photoemission spectroscopy (ARPES) measurements were done at BL-7 in HiSOR. Figure 3(a) shows the wide energy range ARPES images on Si(111) (top) and Si(557) (bottom). Clear bulk bands are observed on Si(111). On Si(557) substrate faint but similar bands that are shifted by 9.5° from the results of Si(111) are observed. Figure 3(b) shows the magnified band structure near the Fermi energy of each sample. A clear V-shaped topological surface state is visualized on Si(111). The observed feature is very similar to the previously reported band structure of Bi_2Te_3/Si(111) films with one quintuple layer (QL) thickness [2]. Thus, the thickness of our film is estimated to be ~1 QL. On Si(557) substrate, similar V-shaped surface state crossing the Fermi energy can be seen, but it was hard to estimate the Fermi momenta (k_F) of surface bands due to the weak intensity. Although we attempted to evaluate the anisotropy of the surface bands by Fermi surface in Fig. 3(c), unfortunately, it was also difficult.

In conclusion, we succeeded to grow Bi_2Te_3 film on silicon vicinal surface and to measure the band structure. However it was difficult to evaluate the band isotropy because of the poor intensity of topological surface states on Bi_2Te_3/Si(557). Further experiment with the better sample quality is expected in the future.
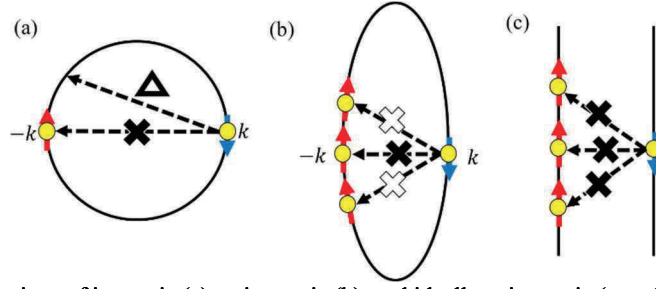
FIGURE 1. Schematic illustrations of isotropic (a), anisotropic (b), and ideally anisotropic (one-dimensional) Fermi surfaces (c) of topological insulator.
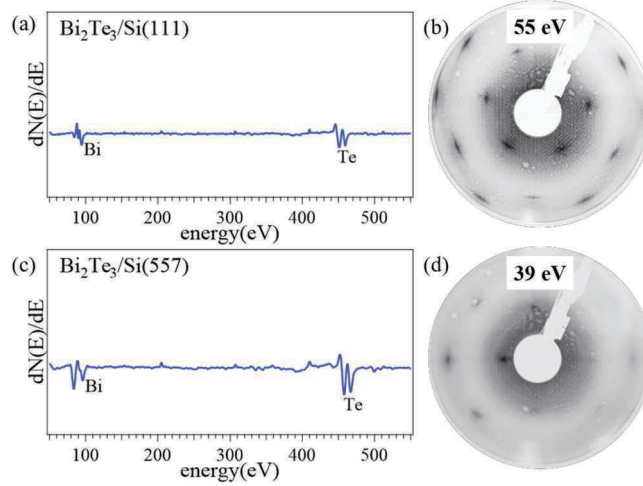

FIGURE 2. (a) AES spectrum of Bi_2Te_3/Si(111)　(b)LEED pattern of Bi_2Te_3/Si(111) taken at 55 eV. (c) AES spectrum of Bi_2Te_3/Si(557)　(d) LEED pattern of Bi_2Te_3/Si(557) taken at 39 eV.
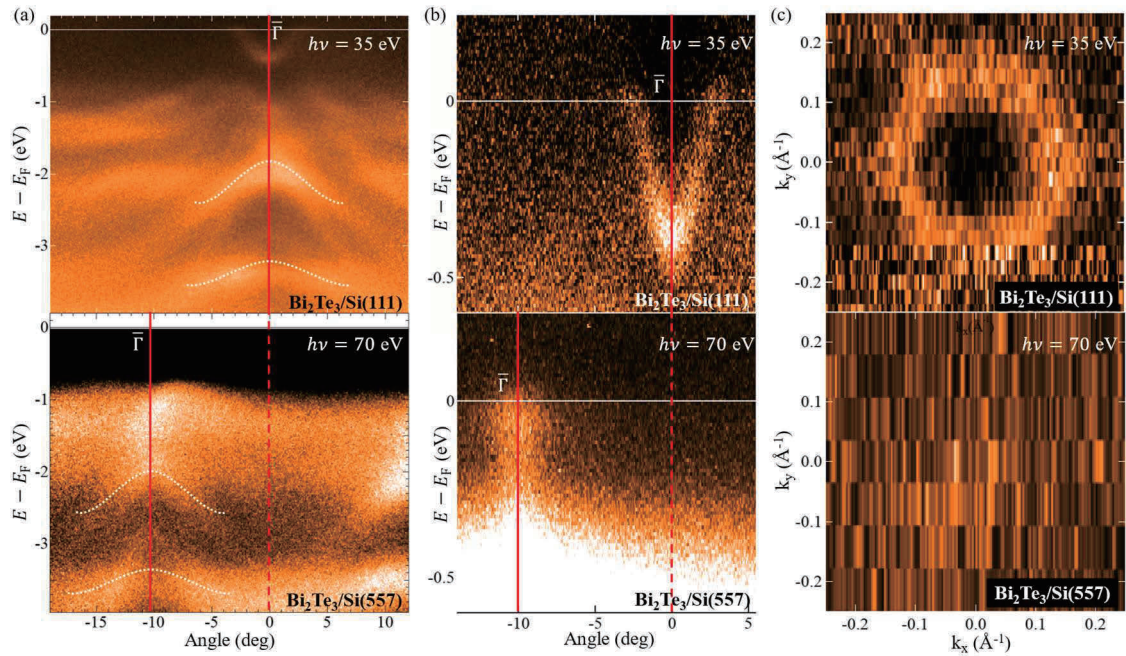
FIGURE 3. (a) Wide range ARPES images of Bi_2Te_3/Si(111) and Bi_2Te_3/Si(557) acquired at $h\nu$ = 35 and 70 eV. (b) Magnified ARPES images around the Fermi energy of (a). (c) Fermi surface of Bi_2Te_3/Si(111) and Bi_2Te_3/Si(557)

REFERENCES

1. N.Nagamura *et al.*, Phys. Rev. Lett. **96**, 256801 (2006).
2. S. Hatta *et al.*, Sci. Rep. **11**, 5742 (2021).

Electronic properties of graphene on Ni(111) substrate investigated by angle-resolved photoemission spectroscopy

Thang Dinh Phan[a], Shingo Takezawa[b], Yukimi Tanimoto[c],
Hitoshi Sato[c,d], Koichiro Yaji[a,e]

[a] *Center for Basic Research on Materials, National Institute for Materials Science (NIMS), Ibaraki 305-0003, Japan*
[b] *Graduate School of Advanced Engineering, Tokyo University of Science, Tokyo 125-8585, Japan*
[c] *Graduate School of Advanced Science and Engineering, Hiroshima University, Hiroshima 739-8526, Japan*
[d] *Hiroshima Research Institute for Synchrotron Radiation Science, Hiroshima University, Hiroshima 739-0046, Japan*
[e] *Unprecedented-scale Data Analytics Center, Tohoku University, Miyagi 980-8578, Japan.*

Graphene is a two-dimensional (2D) graphite with a single layer of carbon atoms arranged in a hexagonal structure. Since the first isolation of graphene from bulk graphite in 2004 [1], graphene has attracted significant interest from scientists because of its special π-π* bandstructure. The conduction and valence bands of graphene symmetrically meet at the charge neutrality point called the Dirac point. The energy of the charge carriers (electrons or holes) is minimal, resulting in unique electronic properties [2], massless Dirac fermions and unusual quantum behavior [3]. These highly mobile electrons between π and π^* orbitals help to enhance the carbon-to-carbon bonds in graphene and drive the electronic properties of graphene, such as carrier concentrations of up to 10^{13} cm^{-2} and charge carrier mobility of $\mu \sim 10,000\ cm^2\ V^{-1}\ s^{-1}$ [1]. At room temperature, this mobility can reach up to 2 x 10^5 cm^{2}V^{-1}s^{-1} [4].

Due to its unique electronic properties, graphene has been considered a possible candidate for future applications, including advancing spin-field effect transistors, spin-based memory devices, oscillators, and logic components. One of the essential steps in utilizing graphene's extraordinary properties is understanding the electronic properties of graphene on the ferromagnetic metal substrate. We focus on studying the electronic structure of graphene on Ni(111) because of the closest matched interface with respect to graphene of Ni(111). An epitaxial-grown monolayer graphene on Ni(111) formed a large gap between the Dirac point and the Fermi level due to the hybridization of the metal d-electrons with the π-orbitals of graphene, making it difficult to control and use the graphene's electrons in devices [5].

In this study, we investigate the electronic structure of chemical vapor deposition (CVD) gown graphene on Ni (111) film prepared on a sapphire (SAP) substrate using angle-resolved photoemission spectroscopy (ARPES). In order to determine the Dirac point and the Fermi level, measurement was conducted near the K point of the π band along the $\overline{\mathit{\Gamma K}}$ direction.

The ARPES experiments were performed at beamline BL7 at the Research Institute for Synchrotron Radiation Science, Hiroshima University. Photon energies of 40-70 eV were used in the experiments. The sample was cooled to approximately 40 K during the measurements.

FIGURE 1 characterizes the observed π band near the Dirac point in graphene on Ni(111) along the $\overline{\mathit{\Gamma K}}$ direction and the energy distribution curves (EDCs) with the photon energy of 40 eV (FIGURE 1 (a)) and 55 eV (FIGURE 1 (b)). The ARPES results demonstrate that the Dirac point is near the Fermi level, resembling the electronic band of pristine graphene. This implies that the charge transfer from the Ni substrate to the graphene is significantly limited.

The π band straight disperses with the binding energy (E_B) of more than 0.5 eV. The electronic properties of CVD-grown graphene on Ni (111) do not change, and the electrons occupying these electronic states behave like they have massless particles at the Dirac point.
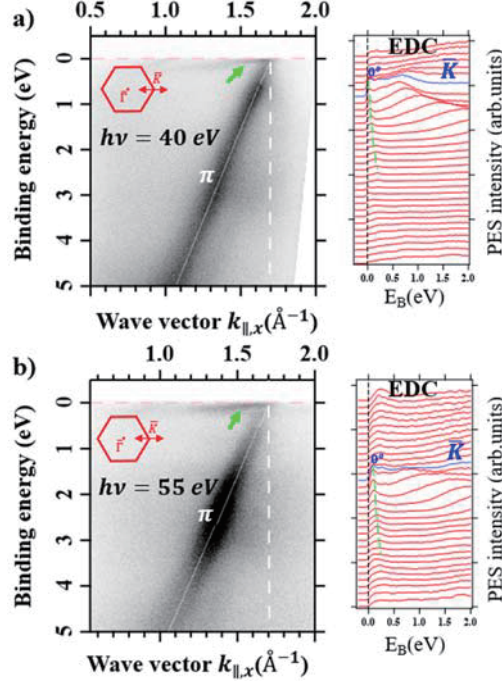
FIGURE 1. ARPES image of graphene on Ni(111) along $\overline{\Gamma K}$ direction.

In FIGURE 1 (a), we can clearly see two nonlinear dispersion points (at $E_B \sim 0.6$ eV and $E_B \sim 2.8$ eV) of the π band when the lower photon energy (40 eV) is used as the excitation energy. While there is only one broadened nonlinear dispersion point (at $E_B \sim 2.8$ eV) that is seen clearly in FIGURE 1 (b).

Additionally, another band is visible near the Fermi level, indicated by the green arrow in both FIGURES 1 (a) and (b), and highlighted by the green dashed line in the right panels. The dispersive feature of this small band is not influenced by the photon energy, which indicates the two-dimensional (2D) intrinsic nature of this band. The interaction between the $2p_z$ states of graphene and the 3d state of Ni metal may induce this band.

In summary, we experimentally observed the electronic states of CVD-grown graphene on Ni(111) using the ARPES technique. As a result, the π band in graphene exhibits the Dirac point near the Fermi level and the linear dispersion with binding energy less than 0.5 eV. Another two-dimensional band is seen near the Dirac point.

REFERENCES

1. K. S. Novoselov et al., *Science*, vol. 306, pp. 666–669, (2004).
2. A. H. Castro Neto, F. Guinea, N. M. R. Peres, K. S. Novoselov, and A. K. Geim, *Rev Mod Phys*, vol. 81, no. 1, pp. 109–162, Jan, (2009).
3. F. Naderi and K. Hasanirokh, *Sci Rep,* vol. 14, no. 1, (2024).
4. A. S. Mayorov et al., *Nano Lett,* vol. 11, no. 6, pp. 2396–2399, (2011).
5. A. Varykhalov *et al.*, *Phys Rev X*, vol. 2, no. 4, (2012).

Probing termination dependent electronic structure in Co-doped LaFeAsO

Soonsang Huh[a], Yuyang Dong[a], Kohei Aido[a], Felix Anger[b], Wurmehl Sabine[b], Bernd Büchner[b, c], and Takeshi Kondo[a]

[a]*The Institute for Solid State Physics (ISSP), The University of Tokyo, Kashiwa, Chiba 277-8581, Japan*
[b] *Leibniz Institute for Solid State and Materials Research, IFW-Dresden, 01069, Dresden, Germany*
[c]*Institute of Solid State Physics, TU Dresden, 01069, Dresden, Germany*

Keywords: Angle-resolved photoemission spectroscopy (ARPES), iron-based superconductor

The discovery of the superconductivity in F-doped LaFeAsO has opened new era for iron-based superconductors and brought renew interest in high T_c superconductivity research [1]. Extensive and intensive studies have shown that the Oxypnictide system, so called 1111 crystal structure system, exhibits relatively high Tc than other systems. Up to now, $SmFeAsO_{1-x}$ ($T_c \sim 55$ K) has been observed with the highest T_c in bulk single crystal at ambient pressure among iron-based superconductors [2]. For this reason, understanding the mechanism that why high T_c favor in this crystal structure becomes one of the main issues in the research field.

In this regard, several angle-resolved photoemission spectroscopy (ARPES) experiments were conducted to understand the electronic structure, which is believed to provide important clues to the high T_C mechanism. However, the 1111 system shows a polarized cleaved surface arising from both the Lanthanide Oxides layer and the Iron Pnictogen layer, resulting in a complex electronic structure. For example, [LaO]+ layer and [FeAs]- layer exist in LaFeAsO. This leads to the coexistence of surface and bulk electronic states. Although previous reports have defined bulk and surface state with several methods, direct evidence of the termination dependence is lacking [3, 4].

In this study, we have performed ARPES measurement on 6% Co-doped LaFeAsO single crystal synthesized by solid state crystal growth technique [5]. Figures 1(a) and (b) show high symmetry cut and its second derivative along $\Gamma - M$ direction, respectively. Near the Γ point, hole bands are observed, which believed to be mainly come from the FeAs layer. Meanwhile, relatively large electron bands are observed near k = -0.4 Å^{-1}. The previous result suggested these electron bands come from the LaO layer [3]. It is noteworthy that the hole band is also observed near the electron bands, which is consistent with the previous result. However, it is difficult to distinguish clearly due to the momentum resolution [3, 4, 6].

To confirm that observed electron bands originate from LaO termination, photon energy-dependent experiments were performed in the range of 8 eV to 40 eV. In Fig. 1(c), electron bands are observed at the all-photon energy range we used. On the other hand, hole bands from the FeAs layer are observed above 12eV. Below 12 eV, the intensity is suddenly suppressed. This result indicates that observed electron bands are from LaO termination and are consistent with the STM result, where large electron bands are expected to exist in the LaO layer [7].
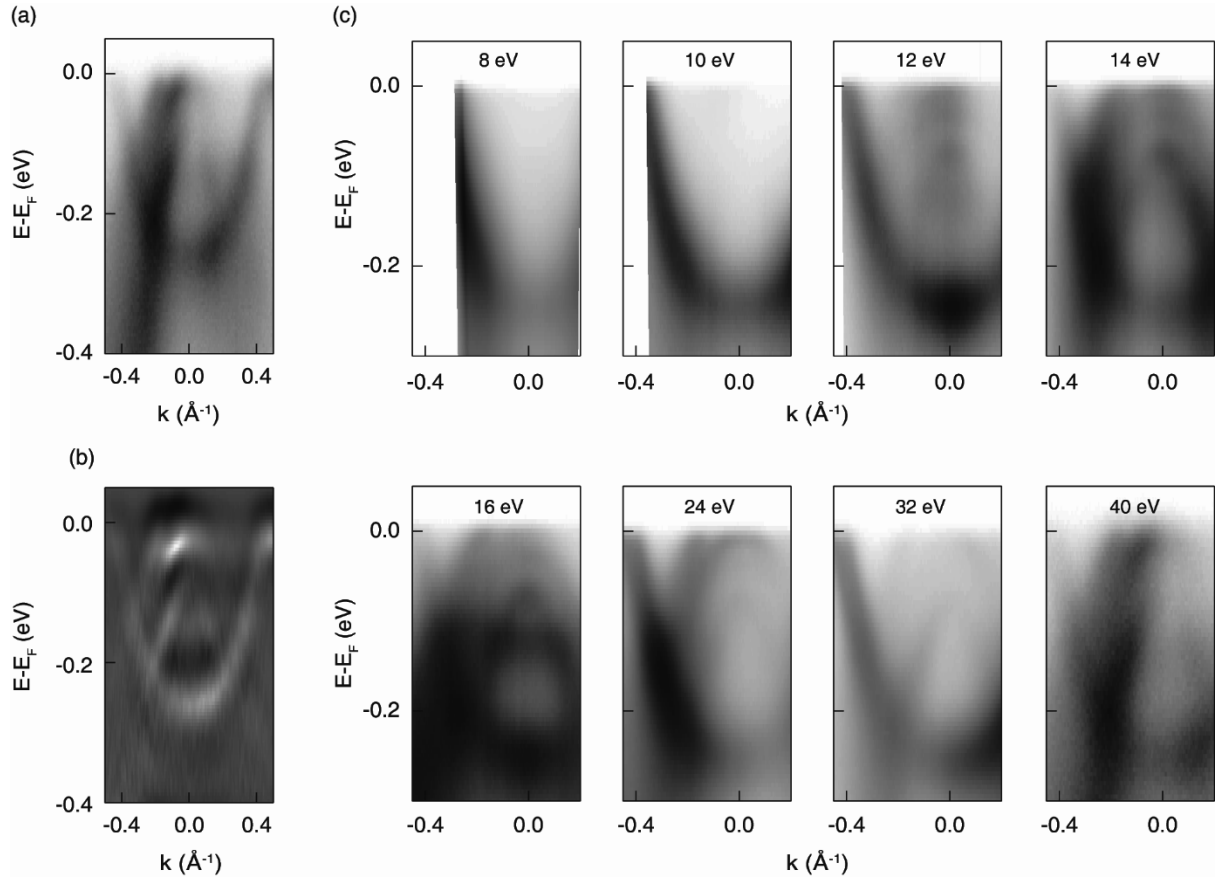
FIGURE 1. (a) High symmetry cut along Γ – M direction and (b) the corresponding second derivative. (c) Cut data taken with various photon energy from 8 eV to 40 eV.

REFERENCES

1. Y. Kamihara, T. Watanabe, M. Hirano, and H. Hosono, J. Am. Chem. Soc. **130**, 3296 (2008).
2. Z.-A. Ren *et al.*, Chin. Phys. Lett. **25**, 2215 (2008)
3. L. X. Yang *et al.,* Phys. Rev. B **82**, 104519 (2010).
4. P. Zhang *et al.,* Phys. Rev. B **94**, 104517 (2016).
5. R. Kappenberger *et al.*, J. Cryst. Growth **483**, 9 (2018).
6. S. Huh *et al.*, Sci Rep **10**, 19377 (2020).
7. X. Zhou *et al.*, Phys. Rev. Lett. **106**, 087001 (2011).

Photoemission Angular Distribution comparing experimental spectra and simulation in the transition metal dichalcogenide 1T -TiS$_2$

Hiroaki Tanaka[a], Shota Okazaki[b], Yuto Fukushima[a], Kaishu Kawaguchi[a], Ayumi Harasawa[a], Takushi Iimori[a], Fumio Komori[c], Masashi Arita[d], Ryo Mori[a], Kenta Kuroda[e, f], Takao Sasagawa[b], and Takeshi Kondo[a, g]

[a]*Institute for Solid State Physics, The University of Tokyo, Kashiwa, Chiba 277-8581, Japan*
[b]*Materials and Structures Laboratory, Tokyo Institute of Technology, Yokohama, Kanagawa 226-8503, Japan*
[c]*Institute of Industrial Science, The University of Tokyo, Meguro-ku, Tokyo 153-8505, Japan*
[d]*Hiroshima Synchrotron Radiation Center, Hiroshima University, Higashi-hiroshima, Hiroshima 739-0046, Japan*
[e]*Graduate School of Advanced Science and Engineering,Hiroshima University, Higashi-hiroshima, Hiroshima 739-8526, Japan*
[f]*International Institute for Sustainability with Knotted Chiral MetaMatter (WPI-SKCM2), Higashi-hiroshima, Hiroshima 739-8526, Japan*
[g]*Trans-scale Quantum Science Institute, The University of Tokyo, Bunkyo-ku, Tokyo 113-0033, Japan*

We develop a simulation process for angle-resolved photoemission spectroscopy (ARPES), in which the photoelectron wave packet that is released is coupled with an outgoing plane wave in a vacuum, represented by a photo-electron wave function. We undertake ARPES measurements on the transition metal dichalcogenide 1T-TiS$_2$, and find good agreement between our calculations and results. Our computed final state wave functions, when analyzed quantitatively, show that the unequal crystal potential and boundary condition cause them to incorporate different waves. These findings indicate that a more thorough examination of the photoelectron final states is required in order to provide a complete explanation for the ARPES spectra that are dependent on photon energy and light polarization.

An increasing body of research has reported on the simulation approaches for the photoemission angular distribution using numerical investigations [1]. While time-dependent density functional theory has been used in the past to simulate ARPES spectra, our focus is on calculating photoemission matrix elements derived from Fermi's golden rule. The simplest form to describe final states is a plane wave; however, some research has included the scattering effects to improve reproducibility [2]. The underlying assumption of these investigations is that a single wavevector is connected to the photoelectron wave function in a solid. The three-step model of photoemission, which describes a photoelectron as a classical particle with a specific momentum, is consistent with this assumption. On the other hand, a photoelectron propagates in a vacuum as a wave packet, a cropped plane wave, according to the time evolution analysis of photoemission [3]. Since photoelectrons behave like waves, we may analyze the entire amplitude of the photoelectron wave packet using time-reversed low-energy electron diffraction (TR-LEED) states, which have been used for decades. Surface-sensitive photoemission analysis requires the TR-LEED wave function to be calculated over the whole thickness of the thick slab, which results in a significant numerical error in the near-surface region. This is because TR-LEED states are defined by the boundary condition at the vacuum layer beneath the slab. Adding an imaginary constant optical potential can help alleviate this problem by causing the photoelectron wave function to rapidly decay into bulk [4]. The exponential decay linked to the constant optical potential, however, is unable to replicate the ARPES spectrum modulation caused by the surface sensitivity, according to a recent ARPES investigation on layered materials [5].

Here, we provide an alternative method for simulating photoemission in the Kohn-Sham system of

density functional theory by limiting the photoelectron wave function to a single outgoing plane wave in the vacuum above the slab using approximations. Our 1-D photoemission simulations validate this approach for eliminating the inbound plane waves. In this case, apart from the traveling wave, the photoelectron wave function inside a solid may contain other waves. The reflected wave must be included in the wave function even in the stepped potential model in order to meet the connection condition at the boundary. We refer to them as first-principles (FP) and plane wave (PW) final states, respectively. As a result, the photoemission angular distribution using such final state wave functions may differ from that using the three-step model wave function, which includes only the traveling wave. We verified our photoemission intensity calculations by contrasting them with the transition-metal dichalcogenide (TMD) 1T-TiS$_2$ ARPES spectra [Figure1]. Although ARPES has studied the electronic structure of TMDs [6], 1T-TiS$_2$ is the best candidate for our investigation due to its readily cleavable quasi-two-dimensional structure, the absence of termination surface dependence consideration [7], and its straightforward electronic structure devoid of the charge density wave phase, in contrast to other 1T-type TMDs [8]. FP final state intensity distributions were shown to be more similar to experimental ones than PW final state intensity distributions. Furthermore, our wave component analysis of FP wave functions showed that they contain other plane waves besides the traveling wave; the absence of these components in the PW final states improved the agreement between simulations and experiments. To the best of our knowledge, our research provides the first quantitative evidence that reflected waves in a solid are included in the final state wave functions. Our work offers an accurate explanation of the photoemission process, which is useful when attempting to derive physical quantities from the distribution of photoemission anomalies.
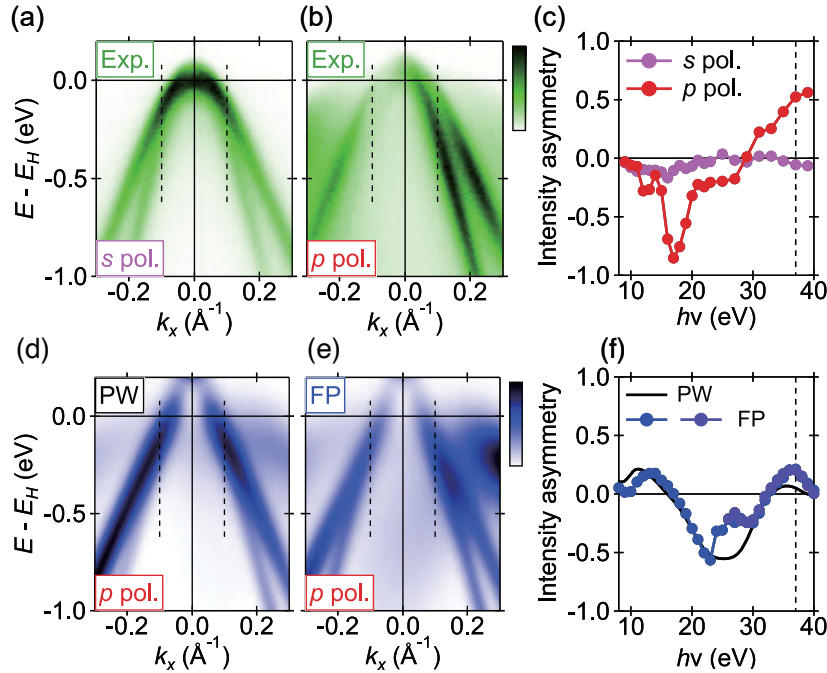

FIGURE 1. Experimental ARPES spectra and simulation results. (a), (b) Experimental spectra along the kx direction taken by s- and p-polarized 37 eV synchrotron lights, respectively. (c) Photon energy dependence of the integrated intensity asymmetry along the dashed lines in (a) and (b). The vertical dashed line is located at $h\nu = 37$ eV. The overlaid curves represent peak positions extracted from energy distribution curves. (d), (e) Simulated photoemission angular distribution using the PW and FP final states. The incident light was 37 eV, p-polarized. (f) Integrated intensity asymmetry calculated from simulated spectra.

REFERENCES

1. R. P. Day et al., npj Quantum Materials 4, 54 (2019)
2. C. S. Kern et al., Phys. Rev. Res. 5, 033075 (2023).
3. H. Tanaka, e-Journal of Surface Science and Nanotechnology 21, 139 (2023).
4. E. E. Krasovskii and W. Schattke, Phys. Rev. Lett. 93, 027601 (2004).
5. H. Tanaka et al., Phys. Rev. Lett. 132, 136402 (2024).
6. W. Jin et al., Phys. Rev. Lett. 111, 106801 (2013).
7. F. Matsui and S. Suga, Phys. Rev. B 105, 235126 (2022).
8. J. A. Wilson, F. J. Di Salvo, and S. Mahajan, Phys. Rev. Lett. 32, 882 (1974).

Observation of quasiparticle peak in the photoemission spectra of quadruple perovskite oxide SrCu₃Ru₄O₁₂

Hiroaki Anzai[a], Yasuaki Kikuchi[a], Yuta Kato[a], Hitoshi Sato[b], Masashi Arita[b],
Ikuya Yamada[a], and Atsushi Hariki[a]

[a] Graduate School of Engineering, Osaka Prefecture University, Sakai 599-8531, Japan
[b] Hiroshima Synchrotron Radiation Center, Hiroshima University, Higashi-Hiroshima 739-0046, Japan

The A-site substituted quadruple perovskite ruthenate ACu₃Ru₄O₁₂ provides a unique opportunity for studying a d-electron heavy-mass behavior. The coefficient of the electron specific heat for the A = Ca compound is $\gamma \sim 84$ mJ/(mol·K²), indicating a heavy effective mass of d electrons [1]. Moreover, the magnetic susceptibility χ shows a broad peak at $T \sim 190$ K [1]. This temperature dependence is quite similar to $\chi(T)$ for CeSn₃, which is a classical $4f$ electron heavy-fermion material [2]. The previous studies have revealed that the hybridization between the localized Cu $3d$ electrons and the itinerant Ru $4d$ electrons is related to the emergence of the Kondo-like peak in the excitation spectra near E_F [3,4]. The first-principles calculation suggests that both Ru-O-Ru and Ru-O-Cu networks contribute to the conducting behavior [5]. Therefore, the band hybridization near E_F should be taken into account for the interpretation of the mass enhancement behavior for A = Ca. We recently synthesized a compound SrCu₃Ru₄O₁₂ under high pressure. The ionic radius of Sr²⁺ is larger than that of Ca²⁺, and thus the lattice expansion occurs with Sr substitution. The change in hybridization strength will provide a new perspective that can detect the primary mechanism responsible for the d-electron heavy-mass behavior.

Here, we present a photoemission spectroscopy study on the quadruple perovskite oxides SrCu₃Ru₄O₁₂. The experiments were performed at BL-9A of Hiroshima Synchrotron Radiation Center. The photoemission data were collected with the photon energy of $h\nu = 16$ eV. The energy resolution was set to 13 meV. The samples were cleaved *in situ* and kept under an ultrahigh vacuum of 6.0×10^{-9} Pa during the measurements.

Figure 1(a) shows the photoemission spectra at $T = 10$ K for the A = Sr compound. Two peaks are observed at $|\omega| \sim 20$ (labeled A) and 80 meV (labeled B). The shapes of the peak A and B are sharper than previously reported
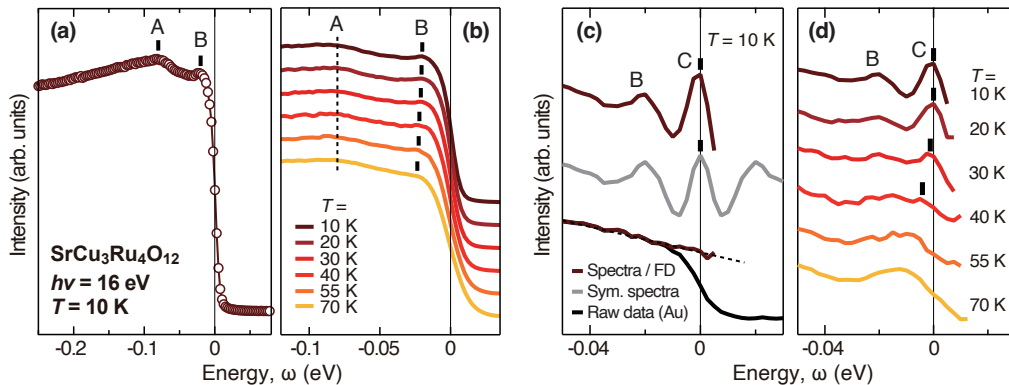

Figure 1. Temperature dependence of the photoemission spectra of SrCu₃Ru₄O₁₂ taken with photon energy of $h\nu = 16$ eV. (a) The photoemission spectra measured at $T = 10$ K. The vertical bars represent the energy positions of the peak A and B. (b) Temperature dependence of the photoemission spectra. (c) Comparison of data analysis between Fermi-Dirac function divided spectra (Spectra/FD) and symmetrized spectra (Sym. spectra). Brown curves indicate spectra of SrCu₃Ru₄O₁₂ and gold (Au) divided by the resolution-convoluted Fermi function. The raw spectra of Au are shown by black curve for comparison. Dashed line is guide to the eye for the Fermi-function divided spectra of Au. Gray curve is the symmetrized spectra of SrCu₃Ru₄O₁₂. (d) Temperature dependence of the Fermi-function divided spectra of SrCu₃Ru₄O₁₂.

spectra on the A = Ca compound [3,4]. We show the temperature dependence of the spectra with vertical offsets in Fig. 1(b), which reveals a temperature evolution of the peak B. In contrast, peak A is insensitive to temperature, implying a different origin to the peak B.

To clarify the lineshape of spectra near E_F, we removed the effect of Fermi-Dirac cutoff on the photoemission spectra near E_F. Figure 1(c) shows a comparison of data analysis between the Fermi-Dirac function (FD) divided spectra and the symmetrized spectra at E_F [6]. The typical metal material of Au shows featureless spectra at T = 10 K. On the other hand, a peak (labeled C) in the spectra of $SrCu_3Ru_4O_{12}$ is located just at the Fermi level. As seen by the FD-divided spectra in Fig. 1(d), the temperature dependence of the energy and intensity for the peak C is similar to that for the peak B, indicating that they share the same origin. It should be emphasized that the enhancement of the peak intensity becomes much more pronounced below T = 30 K. This temperature evolution of peak B and C may be derived from the rapid enhancement of the non-Fermi-liquid properties below 20 K rather than the Kondo effect where the Kondo screening process is practically completed at 300 K [7]. Further investigations such as angle-resolved photoemission measurements are needed for understanding the d-electron based heavy-fermion behavior with the non-Fermi liquid state in $SrCu_3Ru_4O_{12}$.

REFERENCES

1. W. Kobayashi, I. Terasaki, J. Takeya, I. Tsukada, and Y. Ando, J. Phys. Rev. Jpn. **73**, 2373 (2004).

2. T.-W. E. Tsang, K. A. Gschneidner, Jr., O. D. McMasters, R. J. Stierman, and S. K. Dhar, Phys. Rev. B **29**, 4185 (1984).

3. T. Sudayama, Y. Wakisaka, K. Takubo, T. Mizokawa, W. Kobayashi, I. Terasaki, S. Tanaka, Y. Maeno, M. Arita, H. Namatame, and M. Taniguchi, Phys. Rev. B **80**, 075113 (2009).

4. H. Liu, Y. Cao, Y. Xu, D. J. Gawryluk, E. Pomjakushina, S.-Y. Gao, P. Dudin, M. Shi, L. Yan, Y.-F. Yang, and H. Ding, Phys. Rev. B **102**, 035111 (2020).

5. H.-P. Xiang, X.-J. Liu, E.-J. Zhao, J. Meng, and Z.-J. Wu, Phys. Rev. B **76**, 155103 (2007).

6. A. Damascelli, Z. Hussain, and Z. X. Shen, Rev. Mod. Phys. **75**, 473 (2003).

7. T.-H. Kao, H. Sakurai, S. Yu, H. Kato, N. Tsujii, and D.-D. Yang, Phys. Rev. B **96**, 024402 (2017).

Photoemission signature of momentum-dependent hybridization in YbInCu$_4$

Hiroaki Anzai[a], Atsushi Hariki[a], Hitoshi Sato[b], Masashi Arita[b],
Tao, Zhuang[c], and Koichi Hiraoka[c]

[a] *Graduate School of Engineering, Osaka Prefecture University, Sakai 599-8531, Japan*
[b] *Hiroshima Synchrotron Radiation Center, Hiroshima University, Higashi-Hiroshima 739-0046, Japan*
[c] *Graduate School of Science and Engineering, Ehime University, Matsuyama 790-8577, Japan*

Keywords: *c-f* hybridization, Yb compound, photoemission spectroscopy.

The understanding the first-order valence transition in $4f$ systems is one of the most controversial issues of condensed-matter physics. Two nearly degenerate $4f$ valence configurations fluctuate by a small perturbation such as temperature and pressure, and a handful of compounds exhibits a sharp change in their valences at low temperatures [1]. This unusual property is associated with Kondo coupling between the bandlike conduction electrons and the localized $4f$ spin moments, mediated by *c-f* hybridization and *f-f* interaction. The *f-f* interaction strength does not depend on the perturbation. Thus, the experimental challenge for the investigation of the valence transition lies in the observation of the hybridized band dispersions [2].

We focus on the first-order valence transition of the $4f^{13}$ (Yb^{3+}) and $4f^{14}$ (Yb^{2+}) configurations in YbInCu$_4$. The Kondo temperature, which is a measure of the *c-f* hybridization strength, changes from $T_K \sim 25$ K in the high-temperature phase ($T > T_v = 42$ K) to $T_K \sim 400$ K in the low-temperature phase ($T < T_v$) [3]. Mössbauer and x-ray absorption spectroscopy measurements revealed that the Yb valence changes from $z \sim 2.9$ in the high-temperature phase to $z \sim 2.8$ in the low-temperature phase [4]. To understand the mechanism of the valence transition in YbInCu$_4$, we must detect the fingerprints of the *c-f* hybridization.

Here, we report findings of momentum-dependent band dispersions in YbInCu$_4$ by means of angle-resolved photoemission spectroscopy with synchrotron radiation. The experiments were performed at BL-9A of Hiroshima
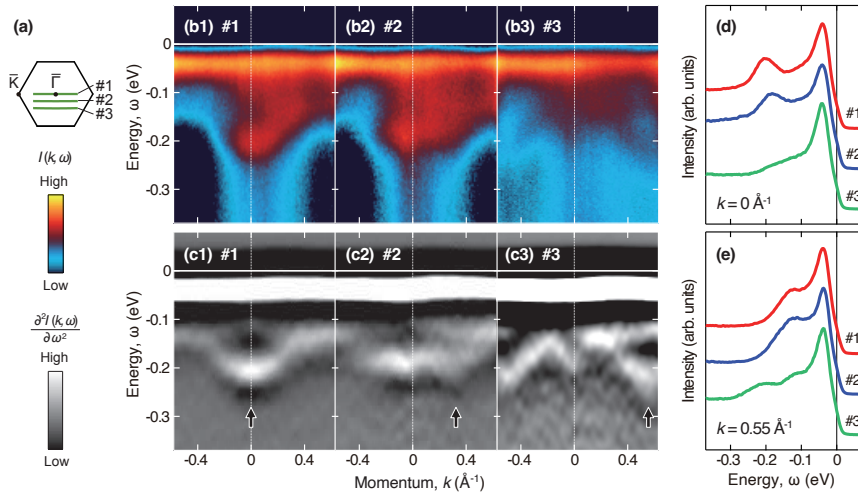

Figure 1. ARPES spectra of YbInCu$_4$ at $T = 10$ K. (a) Schematic figure of the two-dimensional surface Brillouin zone for the (111) crystal plane of YbInCu$_4$. The thick green lines represent the locations of the momentum cuts for #1, #2, and #3. (b1)-(b3) ARPES intensity plot $I(k,\omega)$ taken along three momentum cuts (#1-#3) of two-dimensional surface Brillouin zone, marked by green lines in (a). (c1)-(c3) Second energy derivatives of the ARPES spectra $\partial I(k,\omega)/\partial \omega^2$ for the data set in (b1)-(b3). The black arrows indicate a momentum variation of the band dispersion discussed in the text. (d) Energy distribution curves at $k = 0$ Å^{-1} for the data in (b1)-(b3). (e) The same data set as in (d), but at $k = 0.55$ Å^{-1}.

Synchrotron Radiation Center. The samples were cleaved *in situ* along (111) crystal plane. The data were acquired with $h\nu = 24$ eV photons. The energy resolution was set to 17 meV.

Figure 1(b) shows ARPES spectra $I(k, \omega)$ near E_F along three momentum cuts (#1-#3) of the surface-projected Brillouin zone in Fig. 1(a). The spectra were measured at $T = 10$ K in the low-temperature phase. To identify the shape of bands, the second derivative of the ARPES spectra with respect to energy $\partial I(k,\omega)/\partial \omega^2$ is also plotted in Figs. 1(c1)-(c3). The flat band of the $4f_{7/2}$ state is clearly observed at $|\omega| \sim 0.04$ eV. The corresponding large peak in the energy-distribution curves (EDCs) is seen in Figs. 1(d) and 1(e). We note that the momentum dependence of the $4f_{7/2}$ band at 0.04 eV is negligible within the present experimental resolution.

The bands on the high-energy side of the $4f_{7/2}$ peak have momentum dependence. As shown by spectra along cut #1 in Figs. 1(b1) and 1(c1), the band at $|\omega| \sim 0.13$ eV splits into upper and lower branches around $k \sim 0$ Å^{-1} of the $\bar{\Gamma}$ point. From the peak position of the EDCs in Fig. 1(d), the bottom of the lower branch is estimated to be $|\omega| \sim 0.21$ eV. Similar splits and dispersions of the $4f$ derived bands near the $\bar{\Gamma}$ point were observed in the Yb $4f$ systems and were reproduced by the periodic Anderson model implementing the c-f hybridization. Away from the $\bar{\Gamma}$ point (cuts #1 to #3), an electronlike band leaves the lower branch for the $\bar{M}$ point, as indicated by the arrows in Figs. 1(c1)-1(c3). Interestingly, the lower branch still exists at $k \sim 0$ Å^{-1} in the spectra of cuts #2 and #3, indicating an overlap of the conduction bands at the high-symmetry $\bar{\Gamma}$ point. Such a dentlike shape in $4f$-derived bands has been observed in Yb compounds and is assigned to hybridization phenomena [5,6]. This similarity suggests the hybridization between the $4f$-derived states and conduction bands in YbInCu$_4$.

REFERENCES

1. B. Johansson, Phys. Rev. B **20**, 1315 (1979).
2. C. M. Varma, Rev. Mod. Phys. **48**, 219 (1976).
3. I. Felner, I. Nowik, D. Vaknin, U. Potzel, J. Moser, G. M. Kalvius, G. Wortmann, G. Schmiester, G. Hilscher, E. Grantz, C. Schmitzer, N. Pillmayr, K. G. Prasad, H. de Waard, and H. Pinto, Phys. Rev. B **35**, 6956 (1987).
4. J. L. Sarrao, C. D. Immer, C. L. Benton, Z. Fisk, J. M. Lawrence, D. Mandrus and J. D. Thompson, Phys. Rev. B **54**, 12207 (1996).
5. S. Danzenbächer, Y. Kucherenko, D. V. Vyalikh, M. Holder, C. Laubschat, A. N. Yaresko, C. Krellner, Z. Hossain, C. Geibel, X. J. Zhou, W. L. Yang, N. Mannella, Z. Hussain, Z.-X. Shen, M. Shi, L. Patthey, and S. L. Molodtsov, Phys. Rev. B **75**, 045109 (2007).
6. D. V. Vyalikh, S. Danzenbächer, Y. Kucherenko, K. Kummer, C. Krellner, C. Geibel, M. G. Holder, T. K. Kim, C. Laubschat, M. Shi, L. Patthey, R. Follath, and S. L. Molodtsov, Phys. Rev. Lett. **105**, 237601 (2010).

Electronic structure of noncoplanar antiferromagnet MnTe$_2$ studied by ARPES

Yu-Jie Hao[a], Yu-Peng Zhu[a], Meng Zeng[a], Xiang-Rui Liu[a], Ming-Yuan Zhu[a], M. Arita[b], Chang Liu[a]

[a] Shenzhen Institute for Quantum Science and Engineering (SIQSE) and Department of Physics, Southern University of Science and Technology (SUSTech), Shenzhen 518055, China.
[b] Hiroshima Synchrotron Radiation Center, Hiroshima University, Higashi-Hiroshima, Hiroshima 739-0046, Japan

Mechanisms for spin splitting of electronic bands induced by spin-orbit coupling (SOC) can be classified into two categories: the Zeeman interaction [1] in ferromagnetic materials, and the Rashba-Dresselhaus interaction [2]. The former is characterized by electrons with different spins having equal energy difference regardless of their momentum, whereas the latter has a momentum-dependent energy scale and appears in systems lacking inversion symmetry. Recently, a new type of spin splitting, attributed to long-range magnetic order, has been postulated to occur in certain antiferromagnetic (AFM) materials, even in the absence of SOC [3-6]. This AFM-induced spin splitting is distinctive in that the splitting scale varies upon the momentum of the electrons, and can be considerably larger than the largest known Rashba effect [7]. Despite theoretical calculations predicting compounds like MnTe, CrSb, RuO$_2$ and MnTe$_2$ [8-10] as candidates for such spin splitting, direct spectroscopic evidence remains elusive. In non-coplanar antiferromagnetic MnTe$_2$, the components of spin are predicted to be antisymmetric about the high symmetry planes of the Brillouin zone, forming a "plaid-like" spin texture in the AFM ground state. Specifically, the spin lacks the α component at the $k_\alpha = 0$ ($\alpha = x, y, z$) planes, whereas all components of spin exist when $k_\alpha \neq 0$. To verify this type of spin splitting in MnTe$_2$ using ARPES, it is first necessary to gain an understanding of the relationship between the k_z values and the incident photon energies. Therefore, systematic electronic structure measurements of MnTe$_2$ were performed with different photon energies (11-40 eV) at BL09A. The crystals were cleaved at 30 K (below the Néel temperature of 87 K) and measured at the same temperature.
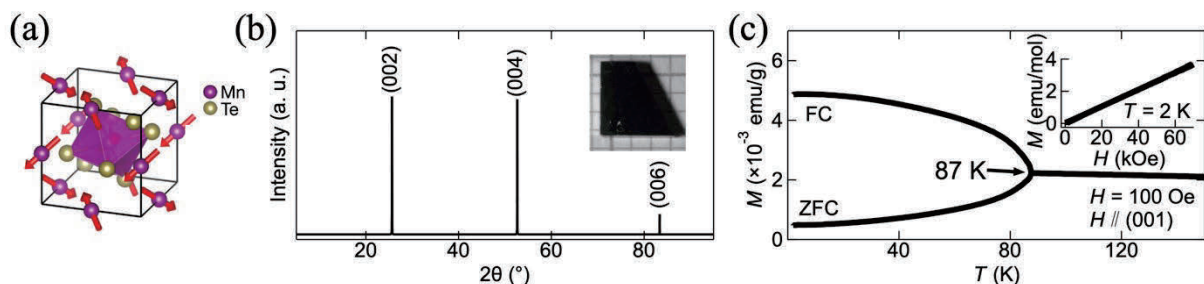

FIGURE 1. Crystal characterization and magnetic responses of MnTe$_2$. (a) Crystal structure of MnTe$_2$ and its noncoplanar AFM magnetic configuration. (b) Single crystal x-ray diffraction data. Inset: A single crystal against a millimeter grid. (c) Field-cooled (FC) and zero-field-cooled (ZFC) temperature dependence of magnetization with $H \parallel (001)$. Inset: magnetic-field dependence of magnetization at $T = 2$ K.

The basic properties of MnTe$_2$ are illustrated in Figure 1. The crystal structure and magnetic structure of MnTe$_2$ are shown in Figure 1(a). Figure 1(b) shows the XRD result and a typical MnTe$_2$ single crystal. Figure 1(c) illustrates the temperature dependence of the magnetization, indicating that the Néel temperature of MnTe$_2$ is 87 K.

The electronic structure of MnTe$_2$ as determined by ARPES at BL09A is illustrated in Figure 2. A detailed photon-energy-dependent ARPES map was conducted, spanning the range from 11 to 40 eV. Figure 2(a) illustrates the k_x-k_z dispersion at binding energies E_B = 0.25 and 0.65 eV, accompanied by the corresponding constant-energy contours calculated by DFT. The experimental spectral intensity is in reasonable agreement with the calculated results, as indicated by the red arrows. Figure 2(b) illustrates the E–k_z dispersion along k_x = 0. Within the scope of our measurement range, the energy band at E_B = 0.5–1.0 eV exhibits repetitive dispersion, which is qualitatively consistent with the dispersion of the theoretical bulk band in terms of dispersion period, bandwidth, and energy positions of band tops. The internal potential is accordingly determined to be V_0 = 10 eV. Based on these results, we can ascertain that $h\nu$ = 21.2 eV corresponds to k_z = 5.8 (-0.2) π/c. This is very important for subsequent spin-resolved ARPES experiments, as a non-vanishing spin signal would be expected under helium-lamp based measurements ($h\nu$ = 21.2 eV) since k_z is not zero there.
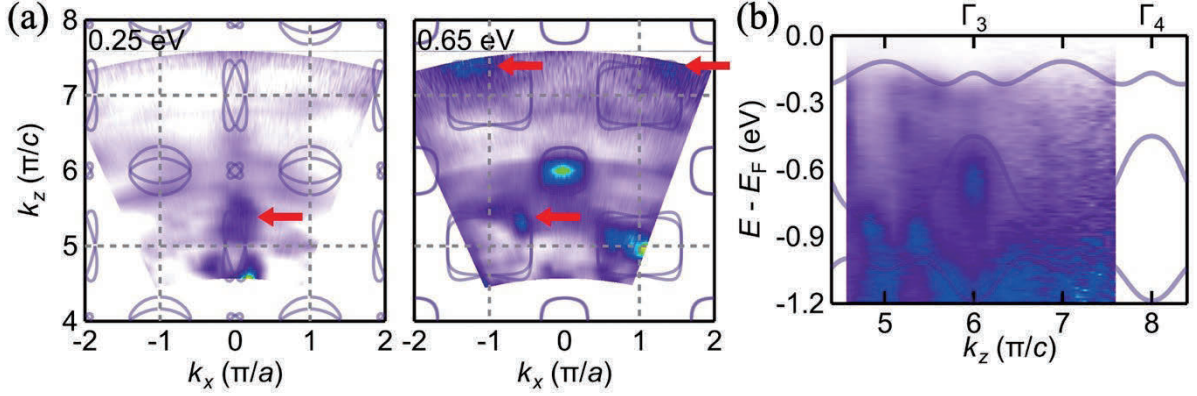

FIGURE 2. Experimental and theoretical results of k_z dispersion of MnTe$_2$. (a) Constant energy contour at binding energy E_B = 0.25 and 0.65 eV. (b) E-k_z dispersion at k_x = 0. Experimental results show a great consistency with the DFT calculated results.

REFERENCES

1. D. Y. Petrovykh *et al.*, *Appl. Phys. Lett.* **73**, 3459–3461 (1998).
2. É. I. Rashba and V. I. Sheka, *Fiz. Tverd. Tela: Collected Papers* **2**, 62–76 (1959).
3. L. D. Yuan *et al.*, *Phys. Rev. B* **102**, 014422 (2020).
4. L. Šmejkal *et al.*, *Sci. Adv.* **6**, eaaz8809 (2020).
5. S. Hayami, Y. Yanagi and H. Kusunose, *J. Phys. Soc. Jpn.* **88**, 123702 (2019).
6. L. Šmejkal, J. Sinova and T. Jungwirth, *Phys. Rev. X* **12**, 031042 (2022).
7. K. Ishizaka *et al.*, *Nat. Mater.* **10**, 521–526 (2011).
8. L. Ishizaka *et al.*, *Phys. Rev. X* **12**, 031042 (2022).
9. L. Šmejkal, J. Sinova and T. Jungwirth, *Phys. Rev. X* **12**, 040501 (2022).
10. L. -D. Yuan *et al.*, *Phys. Rev. Mater.* **5**, 014409 (2021).

Angle-resolved photoemission study of 1T-TaS$_2$ under uniaxial stress

M. Arita

Research Institute for Synchrotron Radiation Science, Hiroshima University,

Keywords: Uniaxial stress, ARPES,

It is possible to control states and induce new phases in materials under external fields such as electric and magnetic fields, as well as pressure. Among these, uniaxial stress can induce lattice modulation and control their electronic states. Recently, angle-resolved photoemission spectroscopy (ARPES) measurements under uniaxial stress have been conducted, establishing this technique as a powerful experimental method [1,2]. To enable such measurements at BL-9A of HiSOR, a sample holder for applying uniaxial stress has been developed (Figure 1).
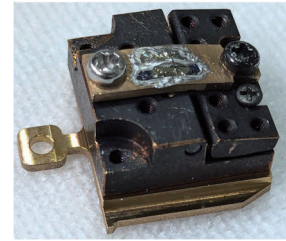

FIGURE 1. Sample holder for applying uniaxial stress using at BL-9A.

Transition-metal dichalcogenide 1T-TaS$_2$ is well known as a layered material that exhibits various charge density wave (CDW) phases: the incommensurate CDW (ICCDW) phase in the temperature range from 550 K to 350 K, the nearly commensurate CDW (NCCDW) phase from 350 K to 180 K, and the commensurate CDW (CCDW) phase below 180 K upon cooling [3,4]. According to electrical resistivity measurements, the transition temperature from the NCCDW to the CCDW phase shifts to lower temperature side under the pressure, and the CCDW phase disappears above 1 GPa [5]. This report investigates how uniaxial stress affects the electronic structure and the CDW transition temperature using ARPES.

Figures 2 (a) and (b) show the ARPES images of 1T-TaS$_2$ with no stress along the Γ-M direction in the ICCDW phase at 370 K and the CCDW phase at 25 K, respectively. The dispersive band structure between E = 0 eV and 1 eV is attributed to Ta 5d, and the band below E = 1 eV is derived from S 2sp. The band structure along Γ-M in the ICCDW phase is similar to that in the normal state, and little modification is observed in the band structure in the NCCDW phase. In the CCDW phase, folding of the Ta 5d band occurs due to the strong the CDW potential, causing the spectral weight of the Ta 5d band to transfer to $k_x \sim 0$ Å^{-1}. Changes in the band structure were not clearly observed in the ARPES spectra for the CDW phase under uniaxial tensile stress along the Γ-M direction.

Figure 2(c) shows the intensities integrated around $k_x = 0$ Å^{-1} in the spectra taken from 370 K to 20 K. The integrated region is indicated by a rectangle in Fig. 1(a). On cooling, a sharp increase in spectral intensity is observed around 170 K both without and with uniaxial tensile stress, indicating the NCCDW to CCDW phase transition. However, the transition temperature is approximately 5 K lower under stress compared to
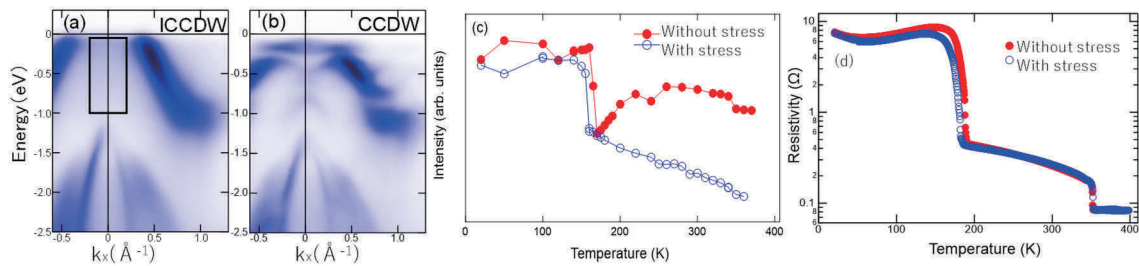

FIGURE 2. ARPES images of 1T-TaS$_2$ along Γ-M without stress in (a) ICCDW and (b) CCDW phases. (c) The spectral intensities integrated over the range indicated by the rectangle in (a) without (solid circles) and with (open circles) uniaxial stress. (d) The electrical resistivities using four-point probe method without (solid circles) and with (open circles) uniaxial stress.

without stress. Using the same sample holder for applying stress, the electrical resistivity was measured on a different sample using the four-point probe method. Figure 1(d) shows the resistivity of 1T-TaS$_2$ without (solid circles) and with uniaxial stress (open circles) on cooling. The direction of the stress is parallel to both the Γ-M and current directions. The resistivities increase steeply around 190 K, indicating the NCCDW to CCDW transition. Stress decreases the transition temperature by about 5 K, showing a trend similar to the result obtained from the ARPES measurement.

It is considered that the decrease in transition temperature between NCCDW and CCDW phases is caused by the suppression of Fermi surface nesting due to uniaxial stress applied to the lattice.

REFERENCES

1. S. Riccò *et al*., Nat. Commun. **9**, 4535 (2018).
2. C. W. Nicholson *et al*., Commun. Mater. **2**, 25 (2021).
3. J.A. Wilson *et al*., Phys. Rev. Lett. **32** 882 (1974).
4. J.A. Wilson *et al*., Adv. Phys. **24** 196 (1975).
5. B. Sipos *et al*., Nat. Mater. **7**, 960 (2008)

Signs of alternative spin polarization in unconventional spin-split antiferromagnet VNb$_3$S$_6$

Meng Zeng[a] and Chang Liu[a]

[a] *Department of Physics and Shenzhen Institute for Quantum Science and Engineering (SIQSE), Southern University of Science and Technology (SUSTech), Shenzhen, Guangdong 518055, China*

Keywords: Spin splitting, unconventional antiferromagnet, spin-resolved ARPES

Magnetic materials play a crucial role in our daily lives. The control of spins in magnetic materials has long been a significant research topic in spintronics [1−3]. Two important parameters of candidate materials are the phase transition temperature and the energy level of spin-splitting. A higher phase transition temperature is more favorable for widespread applications, while a larger spin-splitting strength ensures stable transport properties and facilitates precise control of spin.

Generally, materials with substantial spin-splitting are primarily ferromagnetic materials and those with strong spin-orbit coupling (SOC). The spin-splitting mechanism of the former is mainly the Zeeman effect because of the large net magnetic moment [4,5], while that of the latter is mainly the SOC-induced Rashba or Dresselhaus effects [6,7]. However, strong SOC effects normally present in high-Z materials, which are usually toxic and prone to forming undesirable defects, thereby limiting their applications [8−11].

Recently, it has been discovered that low-Z antiferromagnets also exhibits substantial spin splitting [12–17]. In these systems, the SOC effect is negligible, allowing the degrees of freedom in the spin space and the lattice space to be decoupled, which permits the existence of more special symmetries. To describe these unique symmetries, researchers developed the spin space group theory [18–20]. Chen *et al.* used spin space group theory to categorize antiferromagnets into three types based on the symmetry operation A that simultaneously reverses the spins and exchanges the two sublattices [21]. The antiferromagnet belonging to Type-III ($A = C_n$) has garnered widespread attention due to its significant spin splitting. Due to the magnitude of its spin-splitting being significantly higher than that of known materials [22,23], much purer spin current can be generated, thereby offering broad prospects for applications in spintronics.

In this report, we focus on VNb$_3$S$_6$, a non-collinear antiferromagnet with canted moment along the out-of-plane direction. The research on the peculiar spin texture in VNb$_3$S$_6$ is still in the very early stages and no experiments report the spin polarization of its band structure. Therefore, it is crucial to probe the band spin polarization of VNb$_3$S$_6$ by spin-resolved ARPES. This not only helps to corroborate theoretical predictions but also benefits subsequent research of other candidate unconventional antiferromagnets.

Here, we employ the state-of-the-art spin-resolved ARPES in BL-9B of HiSOR to probe the spin-splitting in VNb$_3$S$_6$. Our data reveals some signs of alternative spin polarization in it. In the experiment, we first set the photon energy to 116 eV ($k_z = 0$) to perform Fermi mappings and align the Γ point, then we change the azimuthal angle and make the exit slit parallel to the Γ-M direction. After that, we set photon energy to 64 eV ($k_z \approx 0.9$ π/c) to perform Fermi mapping again, as shown in Fig. 1(a). Then we set the tilt angle away from 0°, do a k-E cut and carry out the spin polarization measurement on it. The selected position is marked

by the blue dash line and green dots in Fig. 1(a). The k-E cut result is shown in Fig. 1(b), where two hole-type split bands can be observed. In order to check the alternative spin polarization along in-plane directions, we select the momenta on both sides of the Γ point and repeat the spin-EDC measurement. As depicted in Fig. 1(c), we find that the spin polarization is antisymmetric about the high symmetry line $k_x = 0$. This is consistent with the theoretically predicted spin texture, revealing signs of alternative spin polarization in unconventional spin-split antiferromagnet VNb_3S_6. The maximum spin polarization is close to 10%, and is found to be different on different sides of Γ, which we speculate to be resulting from the matrix element effect. The lack of higher levels of spin polarization may be due to the formation of multiple domains that contribute to opposite signs of spin polarization.

Due to limited machine time, we obtained only the above results. However, this data is far from sufficient to verify the alternative spin texture predicted by theory. Subsequently, we need to change the photon energy and rotate the sample to do the spin-resolved measurement to verify the alternative spin texture along both out-of-plane and in-plane directions.
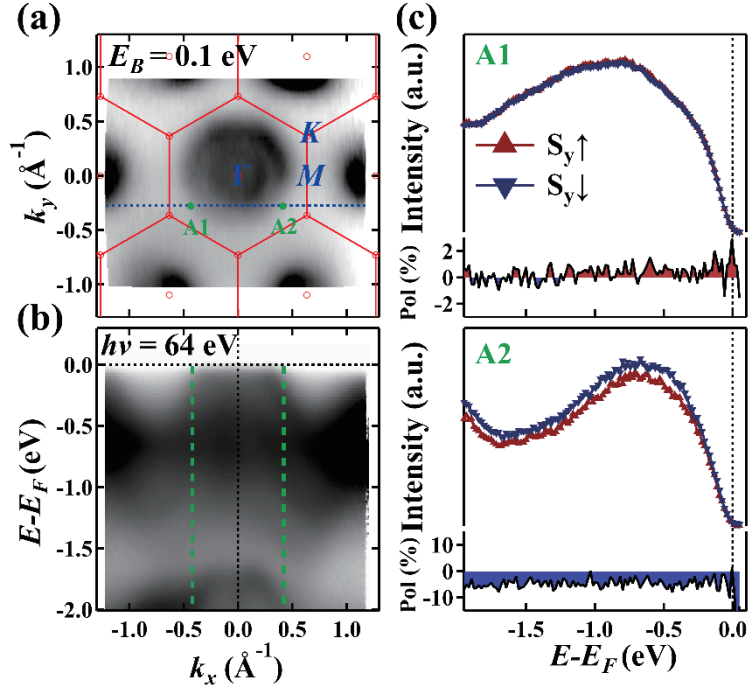

Figure 1. Signs of alternative spin polarization in VNb₃S₆. (a) ARPES constant-energy contour at $E_B = 0.1$ eV with $h\nu = 64$ eV. Red lines and dots mark the 2D Brillouin zone and the high symmetry points. (b) ARPES band dispersion parallel to Γ-M. The green dash lines correspond to the selected energy-distribution curve (EDC) for spin-polarization measurements. (c) Spin-resolved EDCs. Red lines with up-triangle / blue lines with down-triangle correspond to spin-resolved ARPES signals for positive and negative S_y; red and blue areas represent the spin polarization values.

REFERENCES

1. I. Žutić, J. Fabian, and S. Das Sarma, Spintronics: Fundamentals and applications, Rev. Mod. Phys. **76**, 323 (2004).
2. A. Fert. The present and the future of spintronics. Thin Solid Films **517**, 2 (2008).
3. C. Chappert, A. Fert, and F. N. Van Dau, The emergence of spin electronics in data storage, Nature Mater **6**, 813 (2007).
4. P. Zeeman, The effect of magnetisation on the nature of light emitted by a substance, Nature **55**, 1424 (1897).
5. P. Zeeman, XXXII. On the influence of magnetism on the nature of the light emitted by a substance, The London, Edinburgh, and Dublin Philosophical Magazine and Journal of Science **43**, 226 (1897).
6. S. I. Pekar, E. I. Rashba. Combined resonance in crystals in inhomogeneous magnetic fields. Zh. Eksperim. Teor. Fiz.

47 (1964).

7.   G. Dresselhaus, Spin-orbit coupling effects in zinc blende Structures, Phys. Rev. **100**, 580 (1955).

8.   W. A. Harrison. Electronic structure and the properties of solids: the physics of the chemical bond. Courier Corporation, 2012.

9.   T. Taguchi and B. Ray, Point Defects in II－VI Compounds, Progress in crystal growth and characterization **6**, 103 (1983).

10. P. Erhart, D. Åberg, and V. Lordi, Extrinsic point defects in aluminum antimonide, Phys. Rev. B **81**, 195216 (2010).

11. F. Bailly, Energies of formation of metal vacancies in II-VI semiconducting tellurides (HgTe, CdTe, ZnTe), Physica Status Solidi (b) **25**, 317 (1968).

12. L.-D. Yuan, Z. Wang, J.-W. Luo, E. I. Rashba, and A. Zunger, Giant momentum-dependent spin splitting in centrosymmetric low- Z antiferromagnets, Phys. Rev. B **102**, 014422 (2020).

13. L.-D. Yuan, Z. Wang, J.-W. Luo, and A. Zunger, Prediction of low-Z collinear and noncollinear antiferromagnetic compounds having momentum-dependent spin splitting even without Spin-Orbit coupling, Phys. Rev. Mater. **5**, 014409 (2021).

14. L.-D. Yuan, Z. Wang, J.-W. Luo, and A. Zunger, Strong influence of nonmagnetic ligands on the momentum-dependent spin splitting in antiferromagnets, Phys. Rev. B **103**, 224410 (2021).

15. S. Hayami, Y. Yanagi, and H. Kusunose, Spontaneous antisymmetric spin splitting in noncollinear antiferromagnets without spin-orbit coupling, Phys. Rev. B **101**, 220403 (2020).

16. S. Hayami, Y. Yanagi, and H. Kusunose, Momentum-dependent spin splitting by collinear antiferromagnetic ordering, J. Phys. Soc. Jpn. **88**, 123702 (2019).

17. C. Wu, K. Sun, E. Fradkin, and S.-C. Zhang, Fermi liquid instabilities in the spin channel, Phys. Rev. B **75**, 115103 (2007).

18. P. Liu, J. Li, J. Han, X. Wan, and Q. Liu, Spin-group symmetry in magnetic materials with negligible spin-orbit coupling, Phys. Rev. X **12**, 021016 (2022).

19. Ren J, Chen X, Zhu Y, *et al.* Enumeration and representation of spin space groups, arXiv:2307.10369.

20. Z. Xiao, J. Zhao, Y. Li, R. Shindou, and Z.-D. Song, Spin space groups: full classification and applications, arXiv:2307.10364.

21. X. Chen, J. Ren, J. Li, Y. Liu, and Q. Liu, Spin space group theory and unconventional magnons in collinear magnets, arXiv:2307.12366.

22. K. Ishizaka, M. S. Bahramy, H. Murakawa, *et al.* Giant rashba-type spin splitting in bulk BiTeI. Nature mater **10**, 521 (2011).

23. D. Di Sante, P. Barone, R. Bertacco, and S. Picozzi, Electric control of the giant Rashba effect in bulk GeTe, Adv. Mater. **25**, 509 (2013).

Spin-resolved ARPES study on magnetic topological insulator Mn(Bi$_{1-x}$Sb$_x$)$_2$Te$_4$

Xiaoming Ma[a], Shu Mo[a] and Chang Liu[a]

[a] Department of Physics and Shenzhen Institute for Quantum Science and Engineering (SIQSE), Southern University of Science and Technology (SUSTech), Shenzhen, Guangdong 518055, China

Keywords: Magnetic topological material, MnBi$_2$Te$_4$, spin-resolved ARPES

The quantum anomalous Hall effect (QAHE) is a quantized Hall effect that occurs without an external magnetic field. It has attracted tremendous attentions due to its potential applications in electronic and spintronic devices [1]. Magnetism and topological electronic states are two prerequisites for realizing a QAHE state. Magnetic topological insulator (MTI) is considered to be one of the most promising topological matters to realize QAHE. Therefore, the discovery of the first intrinsic magnetic topological insulator MnBi$_2$Te$_4$ immediately attracted widespread attention [2]. MnBi$_2$Te$_4$ is a van der Walls quasi-2D system with the space group R-3m, with a unit cell in which a MnTe layer is inserted into a layer of Bi$_2$Te$_3$ [2]. A magnetic transition between the antiferromagnetic (AFM) ground state and the paramagnetic (PM) state is found around 24 K. Neutron studies reveal that the magnetic moments are ferromagnetically ordered within a MnTe plane, pointing along the out-of-plane *c* direction, but switching sign between adjacent MnTe layers [3,4]. A previous study found that the Fermi level of Mn(Bi$_{1-x}$Sb$_x$)$_2$Te$_4$ can be tuned from the conduction bands to the valence bands by adjusting the atomic ratio *x* of bismuth to antimony [5]. Soon after, our team conducted systematic electronic structure research on Mn(Bi$_{1-x}$Sb$_x$)$_2$Te$_4$ and discovered that Sb doping can not only regulate the Fermi surface of MnBi$_2$Te$_4$ but also cause an energy gap to open in the Dirac cone surface state (SS) [6]. The physical mechanism of this phenomenon remains unclear. Studying the spin polarization of the gapped SS of Mn(Bi$_{1-x}$Sb$_x$)$_2$Te$_4$ is of great significance for understanding the mechanism of the gap opening and future application prospects.
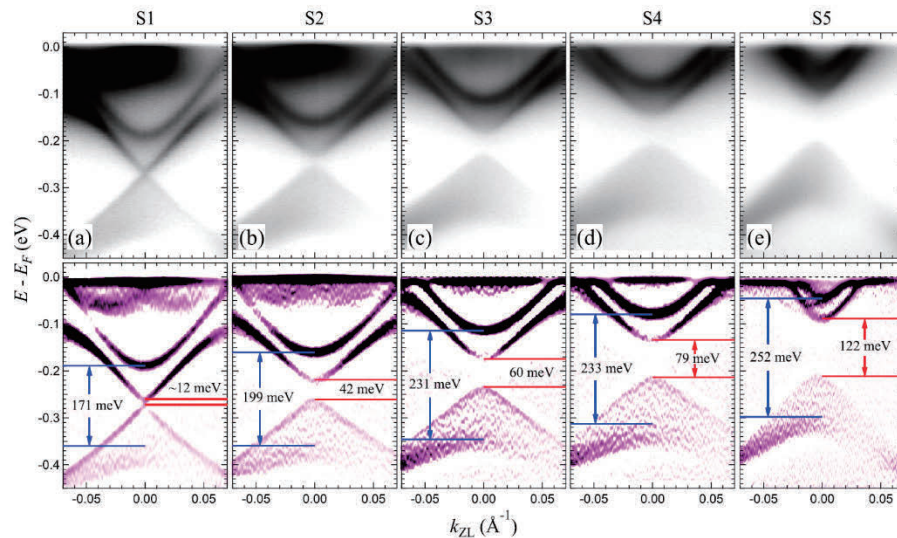

FIGURE 1. ARPES results of Mn(Bi$_{1-x}$Sb$_x$)$_2$Te$_4$. (a)–(e) Raw (top) and second derivative (bottom) ARPES *k-E* maps for five samples with different carrier concentrations ordered by gap size.[6]

We utilized the spin-resolved angle-resolved photoemission spectroscopy (ARPES) setup at BL-9B of HiSOR to investigate the spin polarization of the electronic bands of Mn(Bi$_{1-x}$Sb$_x$)$_2$Te$_4$ during this beamline period. Six Mn(Bi$_{1-x}$Sb$_x$)$_2$Te$_4$ samples with *x* from 0.05 to 0.1 were measured. The normal and spin-resolved ARPES results of Mn(Bi$_{1-x}$Sb$_x$)$_2$Te$_4$ at 10 K are displayed in Fig. 2. According to Ref. [7], the magnetic

topological SS and the non-magnetic topological SS have different spin polarization configurations. The SS of non-MTIs has a helical spin structure and there is no spin component at the Dirac point. The SS of MTIs has a "hedgehog" configuration, and the SS electrons all have out-of-plane spin (S_z) components. Therefore, we focused on the S_z component at Γ for all samples to see whether the situation in Mn(Bi$_{1-x}$Sb$_x$)$_2$Te$_4$ matches the "hedgehog" or the helical spin texture. As presented in Fig. 2, robust opposite S_z polarization near the SS gap can be observed. As shown in Fig. 3, the spin polarization of S2, S3 and S4 do not change at 40 K, which is above the Neel temperature of ~24 K. The controversial results for S1 and S6 will be checked again to rule out artificial problems. We are still collaborating with the theoretical team to conduct in-depth analysis and research on this data.
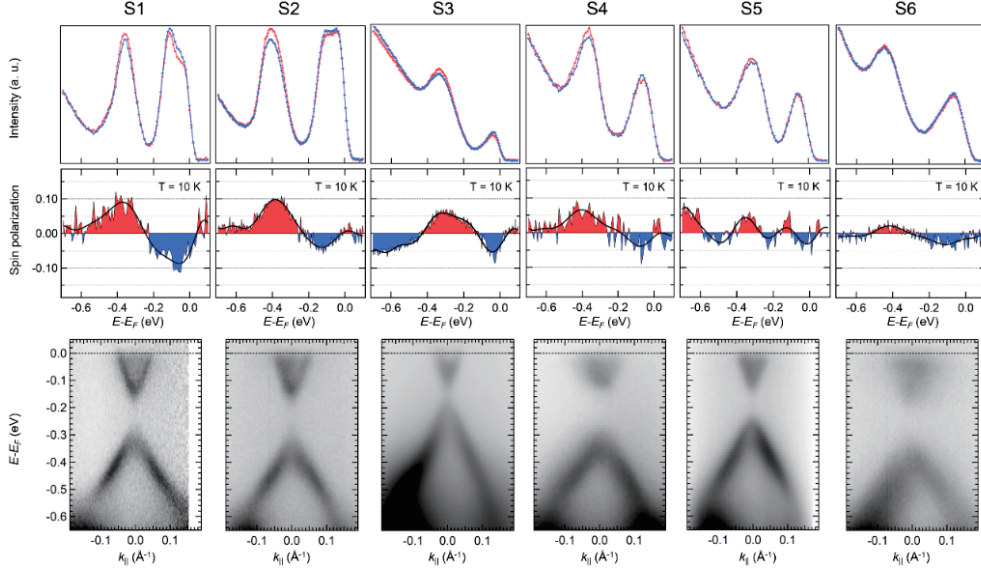

FIGURE 2. Normal and spin-resolved ARPES results of Mn(Bi$_{1-x}$Sb$_x$)$_2$Te$_4$ at 10 K. Rows 1 and 2: the raw spin-resolved EDCs and the corresponding spin polarization curves. Red and blue lines correspond to spin-resolved ARPES signal for positive and negative S_z; red and blue areas correspond to positive and negative S_z polarizations. Row 3: the corresponding normal ARPES E-k cuts.
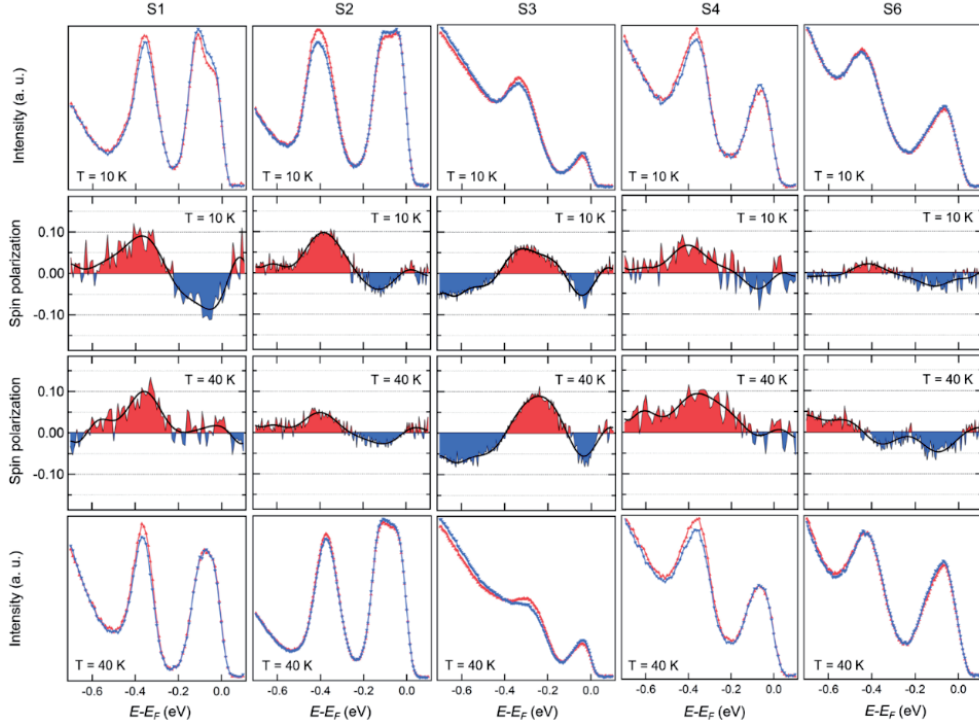

FIGURE 3. Comparison of S_z polarization of Mn(Bi$_{1-x}$Sb$_x$)$_2$Te$_4$ at 10 K and 40 K. Red and blue lines correspond to spin-resolved ARPES signals for positive and negative S_z; red and blue areas correspond to positive and negative S_z polarizations.

REFERENCES

1. M. Z. Hasan and C. L. Kane, Colloquium: Topological insulators, Rev. Mod. Phys. **82**, 3045 (2010).
2. M. M. Otrokov *et al*., Prediction and observation of an antiferromagnetic topological insulator, Nature **576**, 416 (2019).
3. S. H. Lee *et al.*, Spin scattering and noncollinear spin structure-induced intrinsic anomalous Hall effect in antiferromagnetic topological insulator $MnBi_2Te_4$, Phys. Rev. Research **1**, 012011 (2019)
4. J.-Q. Yan *et al.*, Crystal growth and magnetic structure of $MnBi_2Te_4$, Phys. Rev. Materials **3**, 064202 (2019).
5. B. Chen *et al.*, Intrinsic magnetic topological insulator phases in the Sb doped MnBi2Te4 bulks and thin flakes, Nat. Commun. **10**, 4469 (2019).
6. X. Ma *et. al.*, Realization of a Tunable Surface Dirac Gap in Sb-Doped $MnBi_2Te_4$, Phy. Rev. B **103**, L121112 (2021).
7. S.-Y. Xu *et al*., Hedgehog Spin Texture and Berry's Phase Tuning in a Magnetic Topological Insulator, Nat. Phys. **8**, 616 (2012).

Topological proximity effect in Sb/Bi heterojunction studied by spin-resolved ARPES

H. Abe[a], L. Konermann[a], K. Sumida[b], K. Miyamoto[b], T. Okuda[b] and A. Takayama[a,c]

[a]*Department of Physics and Applied Physics, Waseda University,*
Okubo 3-4-1, Shinjuku, Tokyo 169-8555, Japan
[b]*Hiroshima Synchrotron Radiation Center, Hiroshima University,*
Kagamiyama 2-313, Higashi-Hiroshima 739-0046, Japan
[c]*Institute of Multidisciplinary Research for Advanced Materials (IMRAM), Tohoku University,*
Katahira 2-1-1, Aoba-ku, Sendai, Miyagi 980-8577, Japan

Recently, extensive studies have been conducted on topological phase transitions in various materials to better understand intrinsic topological phases and explore potential applications. Group-V semimetals, such as bismuth (Bi) and antimony (Sb), are known to exhibit spin-split surface states, often referred to as topological surface states or Rashba-type spin-splitting, at their surfaces and interfaces. Interestingly, it has been predicted that Bi and Sb undergo topological phase transitions under lattice strain. Although bulk Bi is classified as a topologically trivial material, theoretical predictions suggest that slight lattice strain can induce a transition to a topologically nontrivial semimetal [1]. Indeed, angle-resolved photoemission spectroscopy (ARPES) measurements have reported that Bi thin films with fewer than 200 bilayers (BL) exhibit a topologically nontrivial band structure [2]. For Sb, while freestanding Sb(111) films thinner than 4 BL are topologically trivial [3], bulk Sb is classified as a topologically nontrivial material. Similar to Bi, several studies have predicted that tuning the structural parameters of Sb can induce a topological phase transition [3, 4]. Topological phase transitions driven by epitaxial strain at interfaces are particularly promising for applications because they do not require external fields and are compatible with surface-sensitive experimental techniques. Additionally, understanding the electronic structure of interfacial heterojunctions with spin-polarized states is crucial for fundamental physics.

In this study, we performed spin-resolved ARPES on Sb/Bi heterostructures to investigate the spin state at the interface between Sb and Bi. The measurements were conducted at beamlines BL-9B at the Hiroshima Synchrotron Radiation Center (HiSOR). Given the surface sensitivity of photoelectron spectroscopy, we used ultrathin Sb films (2–3 BL) deposited on Bi thin films as our samples. As a continuation of experiment 22AG033, we investigated the momentum dependence of the spin polarization on the band dispersion near Fermi level (E_F.). The samples were prepared by depositing Sb at room temperature onto Bi thin films grown on Si(111). No annealing process was applied to avoid the formation of $Bi_{1-x}Sb_x$ alloys. The 1×1 surface structure of the Sb/Bi heterostructure was confirmed by low-energy electron diffraction (LEED).

Figure 1 shows the Fermi surface around the $\bar{\Gamma}$ point for a 3BL Sb thin film on Bi(111). We observed circular-shaped electronic pocket centered at the $\bar{\Gamma}$ point and surrounding elongated hole pockets, which are consistent with our previous study [5]. To experimentally clarify the spin-polarized nature of the elongated hole pockets, we conducted spin-resolved ARPES measurements at A-D regions. We also display the near E_F spin-resolved energy distribution curves (SR-EDCs) for in-plane (y) spin components measured in A-D regions. As seen in Fig. 1, the SR-EDCs of the hole band in regions A and B are dominated by the down spin, while the up spin is slightly superior in regions C and D. This indicates that the in-plane spin direction is basically reversed in the two opposite hole pockets across the $\bar{\Gamma}$ point, qualitatively consistent with the Rashba picture. In 22AG033, the spin polarization was observed in the inner electron band, and in this 23AG030 the spin polarization was also observed in the outer hole band. Freestanding ultrathin Sb films are theoretically expected to have no spin-polarized component, suggesting that this observed spin polarization arises from the hybridization of the Rashba states of Bi with the band dispersion the Sb ultrathin films.
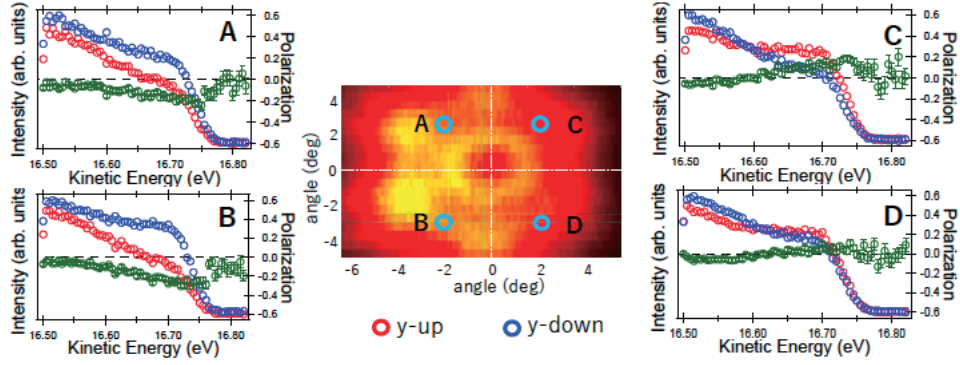
FIGURE 1. The Fermi surface of the 3BL-Sb thin film/Bi(111) around the $\bar{\Gamma}$ point and spin-resolved EDC measured in region A-D, respectively. Green lines show the energy dependence of spin polarization.

REFERENCES

1. T. Hirahara, N. Fukui, T. Shirasawa, M. Yamada, M. Aitani, H. Miyazaki, M. Matsunami, S. Kimura, T. Takahashi, S. Hasegawa, and K. Kobayashi, Phys. Rev. Lett. **109**, 227401 (2012).
2. S. Ito, B. Feng, M. Arita, A. Takayama, R.-Y. Liu, T. Someya, W.-C. Chen, T. Iimori, H. Namatame, M. Taniguchi, C.-M. Cheng, S.-J. Tang, F. Komori, K. Kobayashi, T.-C. Chiang, and I. Matsuda, Phys. Rev. Lett. **117,** 236402 (2016).
3. P. Zhang, Z. Liu, W. Duan, F. Liu, and J. Wu, Phys. Rev. B **85**, 201410 (2012).
4. F.-C. Chuang, C.-H. Hsu, C.-Y. Chen, Z.-Q. Huang, V. Ozolins, H. Lin, and A. Bansil, Appl. Phys. Lett. **102**, 022424 (2013).
5. H. Abe, D. Iwasawa, M. Imamura, K. Takahashi, and A. Takayama, AIP Advances **13**, 055303 (2023).

Electronic Structure and Spin Texture of a Tellurium Kagome Monolayer Grown on Pt(111)

Begmuhammet Geldiyev[a], Philipp Kagerer[a], Jakub Schusser[a], Koji Miyamoto[b],
Taichi Okuda[b,d], Takuma Iwata[c,d], Kenta Kuroda[c,d], Kenya Shimada[b,d],
Maximilian Ünzelmann[a], and Friedrich Reinert[a]

[a]*Experimentelle Physik VII und Würzburg-Dresden Cluster of Excellence ct.qmat*
Universität Würzburg, Am Hubland, D-97074 Würzburg, Germany
[b]*Research Institute for Synchrotron Radiation Science*
Hiroshima University, 2-313 Kagamiyama, Higashi-Hiroshima, Hiroshima 739-0046, Japan
[c]*Graduate School of Advanced Science and Engineering*
Hiroshima University, 1-3-1 Kagamiyama, Higashi-Hiroshima, Hiroshima 739-8526, Japan
[d]*International Institute for Sustainability with Knotted Meta Matter (WPI-SKCM²)*
Hiroshima University, 2-313 Kagamiyama, Higashi-Hiroshima, Hiroshima 739-0046, Japan

In this work, we aim at preparing tellurium (Te) thin films on metallic substrates and measure their electronic band structure with spin resolution. In that regard, our choice of substrate is Pt(111) where once Te coverage reaches 0.44 ML, adatoms form a kagome network with $p(3\times3)$ periodicity upon postannealing the sample approximately at 880 K [1].

Despite our success in achieving the wanted superstructure, the surface electronic band structure as accessed with spin- and angle-resolved photoemission spectroscopy (SARPES) did not show satisfactory results even in spin-integrated mode. In order to realize goals set, we deposited Te this time on Ag(111) and Cu(111) surfaces. On mentioned substrates, Te at 0.33 ML amount creates a binary honeycomb lattice incorporating the respective host elements, which yields AgTe and CuTe [3-5]. In the following, we will present our ARPES results along with spin resolution regarding both systems. Initial spin-ARPES experiments have already been conducted at BL-9B in 2022 (22AG034). However, to finalize the publication, which we are presently preparing, a more systematic study – focusing also on a possible out-of-plane spin twist – is essential.

AgTe and CuTe both have two states in the occupied regime of their surface electronic band structure, namely $\alpha_\pm$ and $\beta_\pm$ as seen in Fig. 1. Energetic difference between the set of bands in those materials set to the side, there is one particular aspect distinguishing the states across. For AgTe, one finds a sizeable Rashba-type in the band $\beta_\pm$ and $\alpha_\pm$ is degenerate, whereas for CuTe no splitting at all could be observed in the spin-integrated ARPES data.

At surfaces, inversion symmetry (IS) is inherently broken, which along with spin-orbit coupling (SOC) leads to Rashba-like spin splittings in the electronic surface band structure [2, 3, 7]. In k-space perspective, this states feature chiral spin texture with in-plane spin polarization that is normal to the momentum direction, the so-called spin-momentum locking. In case of the mentioned scenario, IS is broken in an out-of-plane fashion, and the impact of this is seen in the SARPES measurements for the band $\beta_\pm$ in both AgTe and CuTe (red/blue spectra in Fig. 2). In case of AgTe, the Rashba constant $\alpha_{R} = 0.88 \pm 0.02$ eVÅ was already reported [3], however, we now could quantify the spin-splitting strength to be $\alpha_{R} = 0.24 \pm 0.04$ eVÅ for CuTe as well. The $\alpha_\pm$ band on the other hand, does not show any Rashba component in spin vector in both materials.

Beyond the Rashba effect, it is also viable to break IS perpendicular to the surface normal as this is the instance in binary honeycomb lattices. In turn, this generates out-of-plane spin polarization with contrasting staggered spin orientations across two inequivalent valley momenta K and K′. Particularly, this aspect we are aiming to explore and extend our data systematics to the z component of spin vector. The situation described is alluded to in the spin-resolved data in Fig. 2 (purple/yellow spectra). In stark contrast to the Rashba-type spin polarization (which is almost completely absent for $\alpha_\pm$), there is in fact a finite spin

asymmetry in the z component in the $\alpha_\pm$ and $\beta_\pm$ band. In case of AgTe, the splitting value reads 23 ± 5 meV, and it is 38 ± 2 meV for CuTe.

In conclusion, we report Rashba-like spin splitting emergent in $\beta_\pm$ band for AgTe/Ag(111) and CuTe/Cu(111). It is revealed here first for the latter material system. Moreover, due to the inherent in-plane ISB in such binary honeycomb lattices, there is finite out-of-plane spin polarization along distinct valleys K and K′ [6].
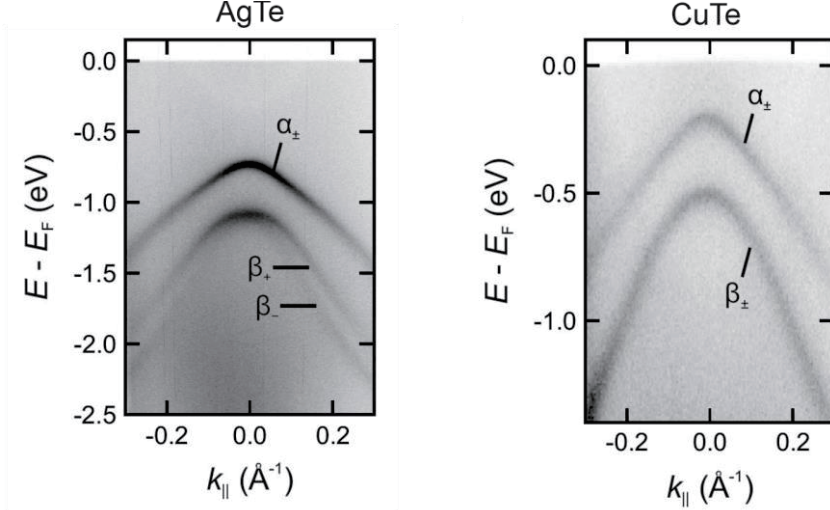

FIGURE 1. ARPES spectra belonging to AgTe is given to the left and that of CuTe to the right. In each case, there exists a pair of states $\alpha_\pm$ and $\beta_\pm$ below the Fermi level. Roughly 0.5 eV shift set aside, electronic band structures are mostly similar. Moreover, the band $\beta_\pm$ features sizeable spin splitting when AgTe is considered, and this is not the occurrence for CuTe in the spin-integrated data above.

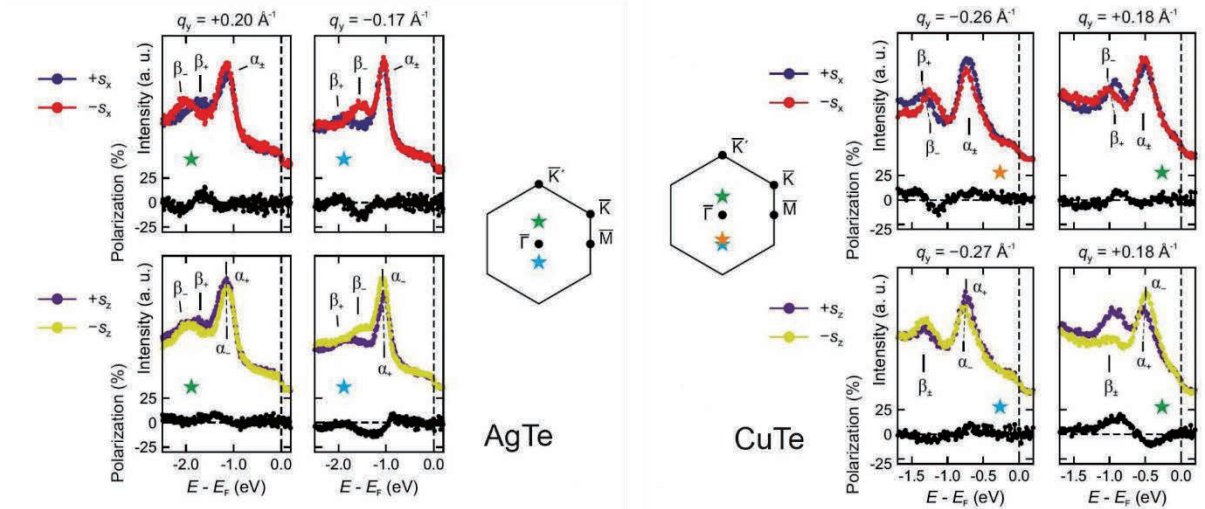**FIGURE 2.** SARPES data summarizing the spin textures observed in AgTe (left column, hv=25 eV) and CuTe (right column, hv=30 eV). In both systems, Rashba-like spin splitting is present for the band $\beta_\pm$, which was thus far not confirmed for CuTe. In addition, out-of-plane valley spin polarization is to be seen in both materials as the result of in-plane ISB emerging from the honeycomb lattice and SOC. Values for the strength of respective spin splittings are provided in the text. Loci where spectra were obtained are given in terms surface Brillouin zone sketches next to respective datasets.

REFERENCES

1. T. Kisslinger et al., *Phys. Rev. B* **108**, 205412 (2023)
2. A. Manchon et al., *Nat. Mater.* **14**, 871-882 (2015)
3. M. Ünzelmann et al., *Phys. Rev. Lett.* **124**, 176401 (2020)
4. Y. Tong et al., *2D Mater.* **7**, 035010 (2020)
5. T. Kisslinger et al., *Phys. Rev. B* **102**, 155422 (2020)
6. B. Geldiyev et al., in preparation (2024)
7. B. Geldiyev et al., *Phys. Rev. B* **108**, L121107 (2023)

Spin-polarized electronic states of FeCo thin film on Rh(001) substrate

K. Kunitomo[a], K. Sumida[b], K. Miyamoto[b], C. Zhang[a],
Y. Sakuraba[c], and T. Okuda[b]

[a]*Graduate School of Advanced Science and Engineering Hiroshima University, 1-3-1 Kagamiyama, Higashi-Hiroshima 739-8526, Japan*
[b]*Hiroshima Synchrotron Radiation Center (HSRC), Hiroshima University 2-313 Kagamiyama, Higashi-Hiroshima 739-0046, Japan*
[c]*National Institute for Materials Science (NIMS), 1-2-1 Sengen, Tsukuba, Ibaraki 305-0047, Japan*

The emergence of perpendicular magnetic anisotropy (PMA) in magnetic thin films is essential from the viewpoint of practical applications, *e.g.*, increasing the recording density of storage devices. Many magnetic thin films exhibiting PMA, such as Co/Pt, Co/Pd, FePt, TbFeCo, and GdFeCo, have been extensively investigated. Among them, "rare-earth and noble-metal elements free" FeCo alloy films are considered promising candidates exhibiting strong PMA. Burkert *et al*. predicted that a magnetic anisotropy energy may increase in FeCo alloys when the tetragonal distortion is applied [1]. Remarkably, around a c/a ratio of 1.20-1.25, the magnetic anisotropy energy exceeds 700-800 μeV/atom, which is one or two orders of magnitude larger than that of pure Fe or Co. The emergence of strong PMA was experimentally confirmed in the tetragonally distorted FeCo ultra-thin-films grown on Rh(001) (c/a = 1.24) with a thickness of 13-17 monolayers (ML) [2].

Generally, it is known that the band structure near the Fermi energy (E_F) plays a very important role in achieving PMA [3,4]. The theoretical calculations suggest that the microscopic origin of PMA in the tetragonally distorted FeCo alloy is attributed to the minority-spin states composed of d_{xy} and $d_{x^2-y^2}$ orbitals near E_F, hybridized by spin-orbit interactions [1]. However, the spin- and orbital-dependent electronic states of the tetragonally distorted FeCo alloy films are poorly investigated experimentally.

In this study, we have fabricated FeCo thin films on Rh(001) substrate by molecular beam epitaxy and investigated the spin-polarized electronic states by *in-situ* spin- and angle-resolved photoemission spectroscopy (spin-ARPES) at BL-9B of Hiroshima Synchrotron Radiation Center [5]. The quality of the sample surface was checked by low energy electron diffraction and Auger electron spectroscopy. The thickness of the film was 13.6 ML. We also carried out the first-principles calculations for the tetragonally distorted FeCo alloy (c/a =1.24) with/without considering the spin-orbit coupling using WIEN2k program [6]. The exchange-correlation was treated using the generalized gradient approximation.

To determine the high symmetry points along k_z direction [Fig. 1(a)], we first performed the photon-energy-dependent measurement. Figure 1(b) shows the ARPES image acquired at various incident photon energies from 45 to 70 eV with *s*-polarization. We can recognize the mostly non-dispersive bands around E_B = 1 eV with k_z = 3.7 Å^{-1} and just below E_F with k_z = 4.4 Å^{-1}. The observed features are reproduced by the calculations (not shown here), and we determined that k_z = 3.6 Å^{-1} (hv = 45 eV) corresponds to the Γ point. Figure 1(c) shows the ARPES image along the Γ-X line recorded at 45 eV with *p*-polarization. A very steep band crossing E_F around the X point is recognized. In addition, weakly dispersive bands are found in between E_F to 1.0 eV around the Γ point.

To experimentally verify the spin-polarization, we next performed the spin-resolved measurements. The sample was magnetized along (001) direction at room temperature prior to the measurements. Figures 2(a) and 2(b) display the out-of-plane spin-resolved energy distribution curves (EDCs) and spin-polarization recorded at the Γ and X points, respectively. Here, red and blue represent the majority- and minority-spin components. For both momenta, we can clearly see the out-of-plane spin-polarization. At the Γ point, we have observed a double peak structure in the minority-spin channel around E_B = 0.2 and 0.6 eV, although the

broad feature can be seen in the wide energy range in the majority-spin channel [Fig. 2(a)]. On the other hand, at the X point, a prominent majority-spin peak exists at E_F [Fig. 2(b)]. These findings tell us that the weakly dispersive bands around the Γ point and the steep band around the X point mainly comprise the majority-spin and majority-spin characters, respectively. Based on the theoretical investigations [2], the majority-spin states composed of d_{xy} and d_{x2-y2} orbitals play an important role in the emergence of the PMA of the tetragonally distorted FeCo films. We finally compare the spin-ARPES results with the first-principles calculations to scrutinize the orbital characters. Figure 2(c) shows the calculated band dispersion along the Γ-X line in the minority-spin channel. The radii of the orange (black) circles are proportional to the net contribution of d_{xy} (d_{x2-y2}) orbital. By a comparison of Figs. 2(a), 2(b) and 2(c), it signifies that the observed minority-spin peak located just below E_F at the Γ point (black arrow) and at 1.1 eV at the X point (orange arrow) are mainly attributed to the d_{x2-y2} and d_{xy} orbitals, respectively.

In summary, we have investigated the spin-polarized electronic states of the FeCo/Rh(001) films by *in-situ* spin-ARPES and first-principles calculations. The out-of-plane spin-polarization indicating the emergence of PMA was clearly observed at room temperature with zero-field. We conclude that the minority-spin states near E_F are mainly composed of d_{x2-y2} and d_{xy} orbitals. Our findings provide the fundamental properties of the FeCo thin films and pave the way for the PMA-based applications, such as the photoelectron spin polarimeter, enabling the detection of the out-of-plane spin components.
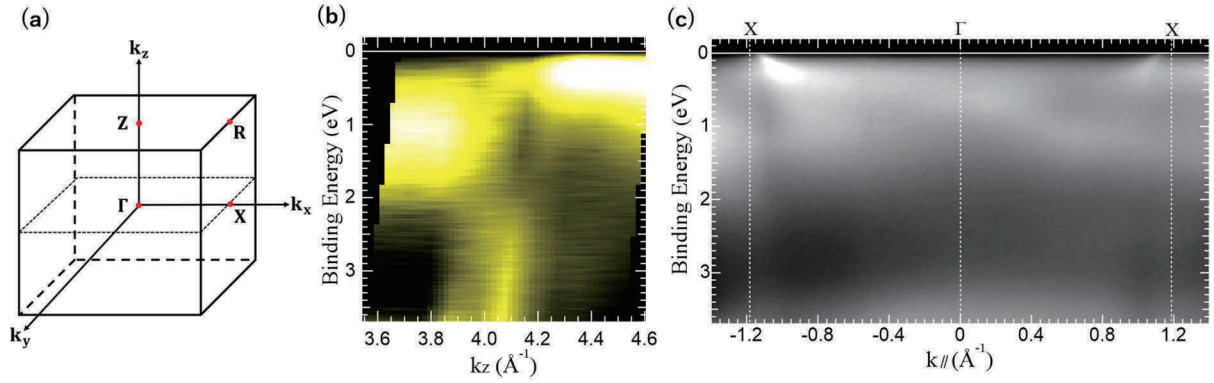

FIGURE1 (a) Brillouin Zone of bct FeCo. **(b)** ARPES image of FeCo/Rh(001) film acquired from 45 to 75 eV with *p*-polarized light. **(c)** ARPES image along the Γ-X line acquired at 45 eV with *p*-polarized light.
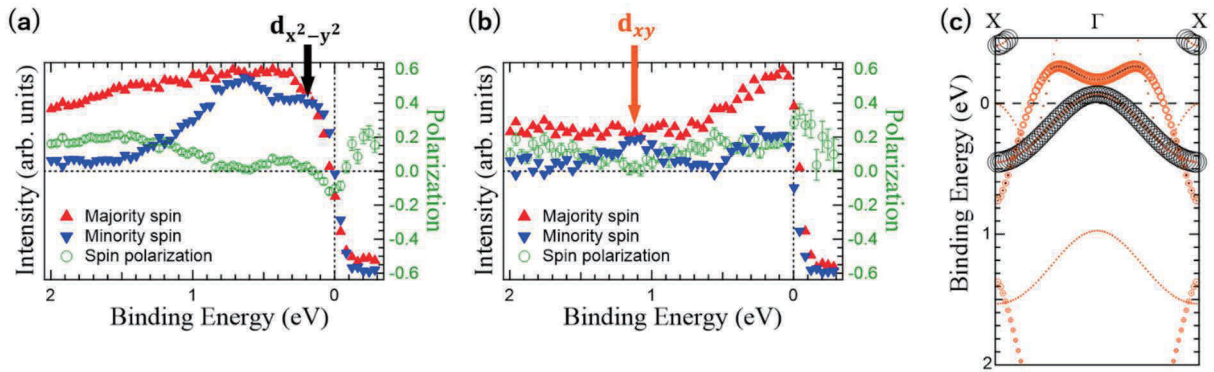

FIGURE2 (a) Out-of-plane spin-EDCs and spin-polarization at the Γ point. **(b)** Same as (a) but at the X point. **(c)** Calculated band dispersion along the Γ-X line in the minority-spin channel. Black and orange represent the d_{x2-y2} and d_{xy} orbitals, respectively.

REFERENCES

1. T. Burkert *et al*., Phys. Rev. Lett. **93**, 027203 (2004).
2. F. Yildiz *et al*., Phys. Rev. B **80**, 064415 (2009).
3. P. Bruno, Phys. Rev. B **39**, 865 (1989).
4. Y. Kota and A. Sakuma, J. Magn. Soc. Jpn. **37**, 17 (2013).
5. T. Okuda *et al*., Rev. Sci. Instrum. **82**, 103302 (2011).
6. P. Blaha *et al*., J. Chem. Phys. **152**, 074101 (2020).

Signs of spin polarization in unconventional spin-split antiferromagnet CrSb

Meng Zeng[a], Xiang-Rui Liu[a], Yu-Peng Zhu[a], Ming-Yuan Zhu[a], K. Miyamoto[b], T. Okuda[b] and Chang Liu[a]

[a] *Department of Physics and Shenzhen Institute for Quantum Science and Engineering (SIQSE), Southern University of Science and Technology (SUSTech), Shenzhen, Guangdong 518055, China*
[b] *Hiroshima Synchrotron Radiation Center, Hiroshima University, Higashi-Hiroshima, Hiroshima 739-0046, Japan*

Keywords: Spin splitting, unconventional antiferromagnet, spin-resolved ARPES

In the framework of group theory, nonmagnetic materials without spin-orbit coupling (SOC), nonmagnetic materials with SOC, and magnetic materials with SOC can be fully characterized by space groups, double space groups, and magnetic double space groups, respectively. However, there are magnetic materials in which SOC can be theoretically set to zero as a starting point to examine the essential physical properties. The symmetry of these magnets is rarely explored. These materials possess a crucial property that the spin degree of freedom is partially decoupled from the orbital part [1-9], resulting in a substantial and momentum-dependent SS whose energy scale is often much larger than that of the SSs caused by SOC. The spin texture of such band splitting remains scarcely measured experimentally [10-15]. To establish the theoretical underpinnings of such innovative antiferromagnets (AFM), Hayami *et al.* proposed that the anisotropic kinetic motion of electrons gives rise to an effective SOC, resulting in an anisotropic SS [10–11]. Yuan *et al.* proposed several prototypes of SS and predicted the presence of AFM-induced spin separation [13-15]. A number of research groups introduced the concept of the spin group [1–9] to describe the electronic structure of such materials, and predicted a series of associated physical phenomena, such as the weak SOC Z_2 topological phase [4], the chiral Dirac-like fermions [16,17], the *C*-pair spin valley locking [18], the non-relativistic spin Hall effect [19,20], the spin splitter torque [21,22], the non-relativistic Edelstein effect [23], and the anomalous Hall effect [24,25]. Specifically, the term "altermagnet" is introduced to designate collinear antiferromagnets that possess such AFM-induced SS [26-28].
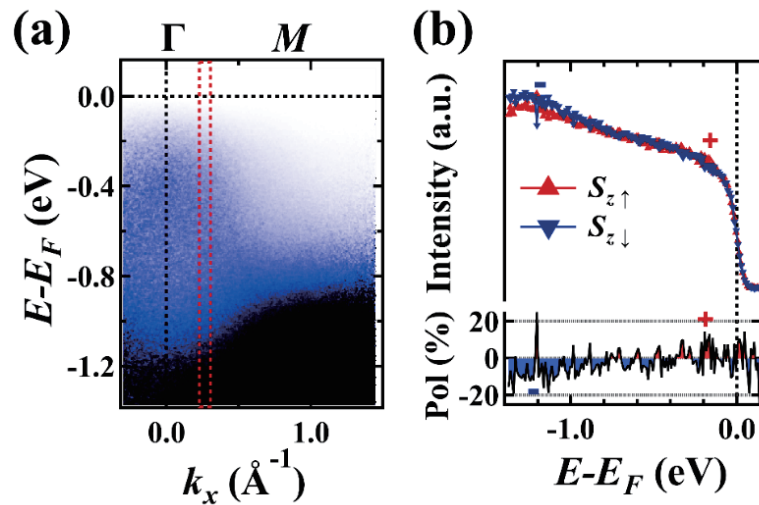

FIGURE 1. Signs of spin polarization in CrSb. (a) ARPES band dispersion parallel to Γ-M with $h\nu = 38$ eV. The red dashed frame corresponds to the selected energy distribution curve (EDC) for spin-resolved ARPES measurement. (b) Spin-resolved EDCs. Red line with upward triangles / blue line with downward triangles correspond to raw intensities of positive and negative spins along the *z*-direction (S_z). Red and blue areas correspond to the corresponding spin polarizations.

In this report, we focus on CrSb, a candidate spin-split antiferromagnet with a Néel temperature significantly surpassing the room temperature. Compared to MnTe, CrSb is an out-of-plane A-type AFM metal, offering better conductivity and magnetic storage density. Compared to RuO_2, CrSb demonstrates higher phase transition temperature, larger effective magnetic moment, and more pronounced anisotropic SS. Hence, CrSb stands out as an ideal material for spintronic application. However, research on the peculiar spin texture in CrSb is still in a very early stage, with few experiments reporting on the spin polarization of its band structure. Therefore, it is crucial to probe the spin polarization of CrSb bands by spin-resolved ARPES. This not only helps to corroborate theoretical predictions but also benefits subsequent research of other candidate materials.

Here, we employ state-of-the-art spin-resolved ARPES in BL-9B of HiSOR to probe the spin-splitting in CrSb. Our data reveals some signs of spin polarization in it.

In the experiment, we first set the photon energy to 72 eV ($k_z = 0$) to perform Fermi mappings and locate the bulk Γ point. Then we adjust the azimuthal angle and make the exit slit parallel to the Γ-M direction. After that, we set the photon energy to 38 eV ($k_z \approx 0.9\ \pi/c$) to do a k-E cut and carry out the spin polarization measurement. The position of the SARPES measurement is marked by the red box in Figure 1(a). As shown in Figure 1(b), we find that the bands at the measure position exhibited some sign of spin polarization up to 10%, and the direction of spin polarization is reversed at different binding energies. This is consistent with the theoretically predicted spin texture, providing evidence for spin polarization in CrSb. The low signal-to-noise ratio in the data may be due to the combined effect of insufficient measurement time and the formation of multiple domains that contribute to opposite spin polarizations.

Due to limited machine time, we obtained only the above result. This data is far from sufficient to verify the alternative spin texture predicted by theory. Subsequently, we need to perform spin-resolved measurements at opposite momentum positions $-k$ at the same incident energy to check if the spin polarization is antisymmetric about the mirror plane. Additionally, we need to change the photon energy and rotate the sample to do the spin-resolved measurement to verify the alternative spin texture along both out-of-plane and in-plane directions.

REFERENCES

1. W. F. Brinkman and R. J. Elliott, *Proc. R. Soc. London, Ser. A* **294**, 343–358 (1966).
2. D. B. Litvin and W. Opechowski, *Physica* **76**, 538–554 (1974).
3. D. B. Litvin, *Acta Crystallogr. Sect. A* **33**, 279–287 (1977).
4. P. Liu, J. Li, J. Han *et al., Phys. Rev. X* **12**, 021016 (2022).
5. X. Chen, J. Ren, Y. Zhu *et al.,* arXiv:2307.10369 (2023).
6. Z. Xiao, J. Zhao, Y. Li *et al.,* arXiv:2307.10364 (2023).
7. J. Yang, Z. –X. Liu and C. Fang, arXiv:2105.12738 (2021).
8. Y. Jiang, Z. Song, T. Zhu *et al.,* arXiv:2307.10371 (2023).
9. X. Chen, J. Ren, J. Li *et al.,* arXiv:2307.12366 (2023).
10. S. Hayami, Y. Yanagi, H. Kusunose, *Phys. Rev. B* **101**, 220403 (2020).
11. S. Hayami, Y. Yanagi and H. Kusunose, *Journal of the Physical Society of Japan* **88**, 123702 (2019).
12. C. Wu, K. Sun, E. Fradkin *et al., Phys. Rev. B* **75**, 115103 (2007).
13. L. -D. Yuan, Z. Wang, J. -W. Luo *et al., Phys. Rev. B* **102**, 014422 (2020).
14. L. -D. Yuan, Z. Wang, J. -W. Luo *et al., Phys. Rev. Mater.* **5**, 014409 (2021).
15. L. -D. Yuan, Z. Wang, J. -W. Luo *et al., Phys. Rev. B* **103**, 224410 (2021).
16. A. Zhang, K. Deng, J. Sheng *et al., Chin. Phys. Lett.* **40**, 126101 (2023).
17. P. Liu, A. Zhang, J. Han *et al., The Innovation* **3**, 100343 (2022).
18. H.-Y. Ma, M. Hu, N. Li *et al., Nat. Commun.* **12**, 2846 (2021).
19. Y. Zhang, J. Železný, Y. Sun *et al., New J. Phys.* **20**, 073028 (2018).
20. H. Watanabe, K. Shinohara, T. Nomoto *et al., Phys. Rev. B* **109**, 094438 (2024).
21. H. Bai, L. Han, X. Y. Feng *et al., Phys. Rev. Lett.* **128**, 197202 (2022).
22. S. Karube, T. Tanaka, D. Sugawara *et al., Phys. Rev. Lett.* **129**, 137201 (2022).
23. R. González-Hernández, P. Ritzinger, K. Výborný *et al.,* arXiv:2310.06499 (2023).
24. Z. Feng, X. Zhou, L. Šmejkal *et al., Nat. Electr.* **5**, 735–743 (2022).
25. N. J. Ghimire, A. S. Botana, J. S. Jiang *et al., Nat. Commun.* **9**, 3280 (2018).
26. L. Šmejkal, J. Sinova and T. Jungwirth, *Phys. Rev. X* **12**, 031042 (2022).
27. I. Mazin, *Phys. Rev. X* **12**, 040002 (2022).
28. I. Mazin, *Physics* **17**, 4 (2024).

Spin-resolved ARPES study on a layered d-wave room-temperature altermagnet $Rb_{1-\delta}V_2Te_2O$

Fayuan Zhang[1*], Xingkai Cheng[2*], Changchao Liu[3*], Zhengtai Liu[4], Mao Ye[4], Cheng Zhang[5], Taichi Okuda[6], Kenya Shimada[6], Guang-Han Cao[3], Junwei Liu[2] and Chaoyu Chen[1,7]

[1] Shenzhen Institute for Quantum Science and Engineering, Southern University of Science and Technology, Shenzhen, China.

[2] Department of Physics, The Hong Kong University of Science and Technology, Hong Kong, China.

[3] Department of Physics, Zhejiang University, Hangzhou, China.

[4] Shanghai Synchrotron Radiation Facility, Shanghai Advanced Research Institute, Chinese Academy of Sciences, Shanghai, China

[5] Graduate School of Advanced Science and Engineering, Hiroshima University, Higashi-Hiroshima, Hiroshima, Japan.

[6] Research Institute for Synchrotron Radiation Science (HiSOR), International Institute for Sustainability with Knotted Chiral Meta Matter (WPI-SKCM2) and Research Institute for Semiconductor Engineering (RISE), Hiroshima University, Higashi-Hiroshima, Hiroshima, Japan.

[7] Institute of Advanced Science Facilities, Shenzhen, China

Theoretical efforts have recently predicted unconventional antiferromagnets characterized by crystal symmetry C (rotation or mirror), which connects antiferromagnetic sublattices in real space and couples spin and momentum in reciprocal space [1]. This results in unique C-paired spin-valley locking (SVL) and novel properties like piezomagnetism and noncollinear spin current without spin-orbit coupling. However, reported unconventional antiferromagnets are not layered, limiting their spintronic application potential and not meeting symmetry requirements for nonrelativistic spin current.

We present the realization of C-paired SVL in a layered room-temperature antiferromagnetic compound, $Rb_{1-\delta}V_2Te_2O$ [2]. DFT-calculation show opposite spin splitting between C-paired valleys. In this study, we validate the presence of spin polarized band structure using spin-resolved ARPES. This marks the first realization of layered antiferromagnets with C-paired

SVL, combining layered material advantages with potential crystal symmetry manipulation control. These findings promise significant advancements in magnetism, electronics, and information technology.
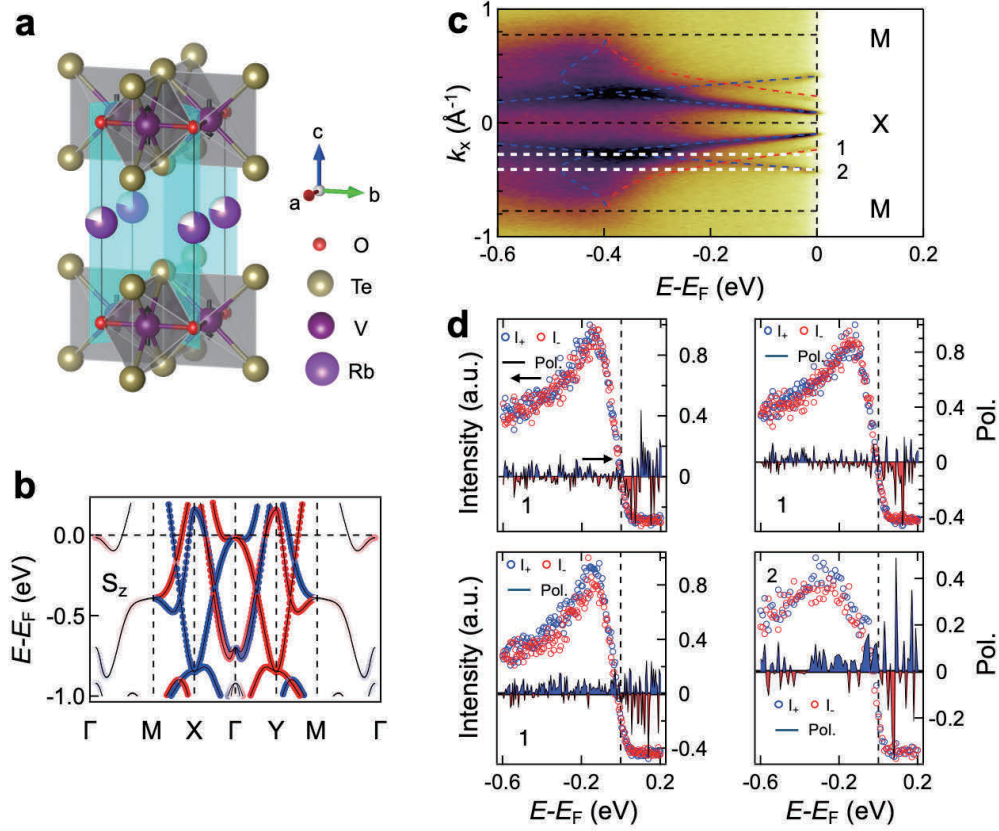

Fig. 1. Spin-resolved ARPES on Rb$_{1-\delta}$V$_2$Te$_2$O. a, Schematic lattice structure of Rb$_{1-\delta}$V$_2$Te$_2$O, where black arrows indicate the magnetic moments of V which are parallel/antiparallel to the c axis. Two magnetic sublattices are related by diagonal mirror symmetry M_1 and M_2 (transparent blue planes) and four-fold rotation symmetry (C_{4z}). **b,** DFT-calculated band structure, blue and red dotted lines are bands with spin up and down, respectively. **c,** ARPES cut along M-X-M, with overlaid blue and red dashed lines representing DFT-calculated bands. **d,** Spin-resolved energy distribution curves (blue and red circles, left), and spin polarization (black solid line, right) corresponding to white dashed lines 1 and 2 marked on c.

REFERENCES

1   Ma, H. Y. *et al.* Multifunctional antiferromagnetic materials with giant piezomagnetism and noncollinear spin current. *Nat Commun* **12**, 2846, (2021).

2   Ablimit, A. *et al.* Weak metal-metal transition in the vanadium oxytelluride Rb$_{1-\delta}$V$_2$Te$_2$O. *Phys Rev B* **97**, 214517 (2018).

Ultrafast Spin-Dependent Dynamics in a Carrier-Tuned Topological Insulator

K. Sumida[a], K. Kunitomo[b], M. Kakoki[b], K. A. Kokh[c], O. E. Tereshchenko[c],
J. Reimann[d], J. Güdde[d], U. Höfer[d], K. Miyamoto[a], T. Okuda[a,e], and A. Kimura[b,e]

[a]*Hiroshima Synchrotron Radiation Center, Hiroshima University, 2-313 Kagamiyama,
Higashi-Hiroshima 739-0046, Japan*
[b]*Graduate School of Advanced Science and Engineering, Hiroshima University, 1-3-1 Kagamiyama,
Higashi-Hiroshima 739-8526, Japan*
[c]*Physics Department, Novosibirsk State University, ul. Pirogova 2, 630090 Novosibirsk, Russia*
[d]*Department of Physics and Materials Sciences Center, Philipps-University, D-35032 Marburg, Germany*
[e]*International Institute for Sustainability with Knotted Chiral Meta Matter (SKCM^2), 1-3-1 Kagamiyama,
Higashi-Hiroshima 739-8526, Japan*

Keywords: Topological insulator, Time-resolved ARPES, Spin-resolved ARPES, Ultrafast carrier dynamics, Spin texture.

Topological insulators (TIs) characterized by spin-polarized Dirac-cone-like band structures on their surfaces have been extensively investigated over the last decade. As a hallmark of TIs caused by strong spin-orbit coupling, the spin-momentum-locked topological surface state (TSS) offers a pure spin current on their surfaces. The spin-polarized surface electrons of TIs are robust against nonmagnetic impurities and defects. So far, many TIs, such as Bi_2Se_3, Bi_2Te_3, and Sb_2Te_3, have been theoretically predicted and experimentally verified by angle-resolved photoemission spectroscopy (ARPES) with spin-resolution.

Recently, the ultrafast optical response of TSS has attracted much attention. Time-resolved ARPES utilizing femtosecond-laser reveals several characteristics and functionalities, *e.g.*, the emergence of Floquet state [1], population inversion [2], and the surface photovoltage effect [3]. However, the ultrafast carrier dynamics derived from the unique spin texture of TSS have hardly been investigated.

In this work, we investigated the spin-dependent ultrafast surface carrier dynamics of a ternary topological insulator $(Sb,Bi)_2Te_3$, where the Dirac point is adjusted to the Fermi energy (E_F), by a combination of laser-based time-resolved ARPES and synchrotron-based spin-resolved ARPES techniques. The pump-probe time-resolved ARPES measurements were performed at Philipps University of Marburg. We used two different pump energies: mid-infrared (MIR) at 0.30 eV and visible (VIS) at 2.58 eV [Figs. 1(a) and 1(d)]. We used an ultraviolet (UV) at 5.16 eV light as the probe. The spin-resolved ARPES measurements, utilizing very low energy electron diffraction type spin-polarimeters, were performed at ESPRESSO end-station (BL-9B) of Hiroshima Synchrotron Radiation Center [4].

Figure 1(b) shows the ARPES image recorded at temporal overlap ($t = 0$ ps) with the MIR-pump. We can recognize the Dirac-cone-like TSS and bulk conduction band above E_F. We also notice that the photoemission intensities
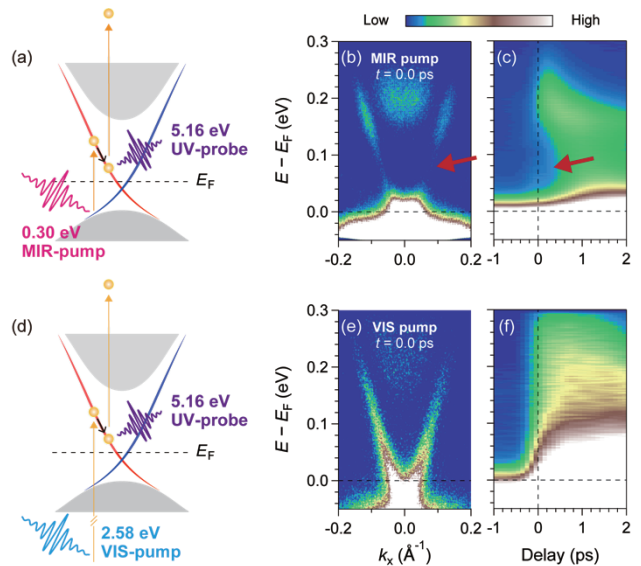

FIGURE 1. (a) Schematic illustration of time-resolved ARPES experiment using MIR-pump and UV-probe. (b) ARPES image of $(Sb_{0.57}Bi_{0.43})_2Te_3$ along $\bar{\Gamma} - \bar{K}$ direction recorded at $t = 0$ ps. (c) Photoemission intensity profile as a function of delay time. (d-f) Same as (a-c) but using VIS-pump.

at the TSS in a certain energy region around 0.05 eV are very weak [see the red arrow in Fig. 1(b)], while those around 0.15 eV are pronounced. To illustrate the temporal evolution of the bands, Figure 1(c) displays the momentum-integrated photoemission intensity profile as a function of delay time. We find a dip structure around 0.05 eV from 0.0 to 0.5 ps. After 0.5 ps, the intensity around 0.05 eV drastically increases because the photo-excited electrons at higher energy states relax through intra-band and inter-band scatterings. These findings suggest that the direct transition is prohibited around 0.05 eV in the MIR-pump scheme. To compare the ultrafast carrier dynamics, we also performed time-resolved ARPES using the VIS-pump [Figs. 1(e) and 1(f)]. However, in sharp contrast to the MIR-pump scheme, no dip structures are visible at $t = 0$ ps.

Since the forbidden transition observed in the MIR-pump scheme likely stems from the unique spin texture of the TSS, we proceeded with the spin-resolved measurement of the occupied bands below E_F. Figure 2(a) shows the spin-resolved ARPES image captured at 17.0 eV. Red and blue colors correspond to positive and negative in-plane spin-polarization, respectively. From E_F to -0.3 eV, the spin-polarized lower portion of TSS is evident. Additionally, M-shaped spin-split Rashba bands are observed around -0.5 eV. Since the directions of in-plane spin-polarization at the upper and lower TSSs are reversed with respect to the Dirac point, the forbidden transitions in the "resonant" MIR-pump scheme are most likely caused by the intrinsic spin texture of TSS, as depicted in Fig. 2(b). In the VIS-pump scheme, on the other hand, the direct transition to the upper TSS is allowed because the transition occurs from the unpolarized deeper-lying bulk continuum states. Finally, we discuss why the direct transition is permitted around 0.15 eV at the TSS in the MIR-pump scheme [Fig. 1(b)]. The upper panels of Fig. 2(c) show the constant energy contours recorded at $t \sim 0$ ps with VIS-pump. At 0.05 eV, an isotropic shape contour is seen. On the other hand, at 0.15 eV, the contour shape undergoes deformation from circular to hexagonal due to the warping effect. On the warped bands, it is known that not only in-plane but also out-of-plane spin components emerge [the lower panels of Fig. 2(c)] [5]. In such a case, the direct transition would be partially allowed.

In conclusion, we have experimentally demonstrated the spin-dependent forbidden transition in the TI by using time-resolved ARPES and spin-resolved ARPES. Our findings pave the way for ultrafast opto-spintronic applications using the TSS of TIs.
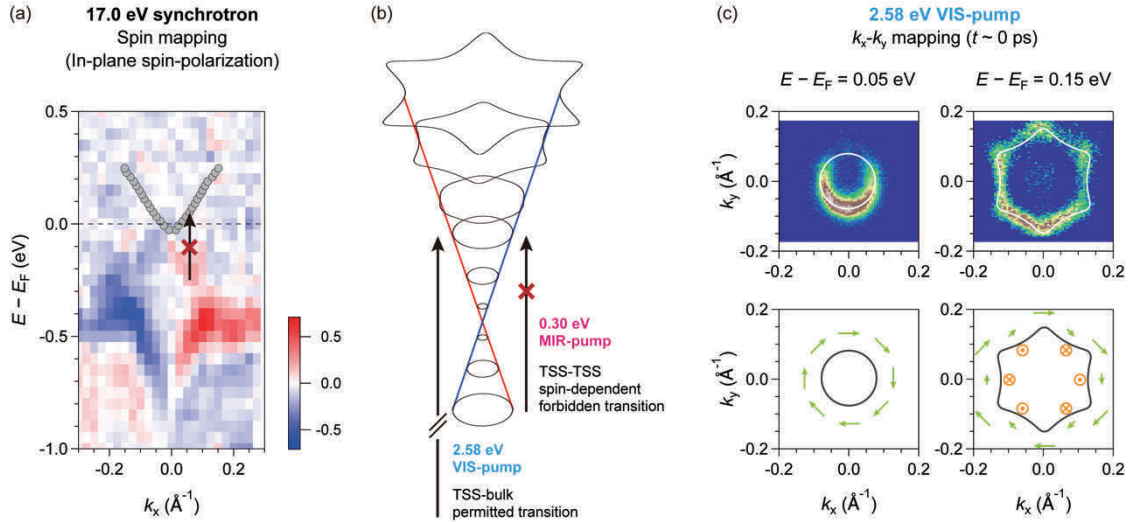

FIGURE 2. (a) In-plane spin-polarization mapping of $(Sb_{0.57}Bi_{0.43})_2Te_3$ along $\overline{\Gamma} - \overline{K}$ direction recorded at 17.0 eV. Gray circles represent the fitting results of the TSS shown in Fig. 1(e). (b) Schematic illustration of spin-dependent direct transition using MIR- and VIS-pump schemes. (c) Upper panel: constant energy contours at 0.05 and 0.15 eV recorded at $t \sim 0$ ps with VIS-pump. Lower panel: Schematic illustrations of spin texture of isotropic (left) and anisotropic TSS (right). Light green and orange colors correspond to the in-plane and out-of-plane spin components, respectively.

REFERENCES

1. Y. H. Wang *et al.,* Science **342**, 453 (2013).
2. S. Y. Zhu *et al.,* Sci. Rep. **5**, 13213 (2015)., K. Sumida *et al.*, Phys. Rev. B **99**, 085302 (2019).
3. K. Sumida *et al.*, Sci. Rep. **7**, 14080 (2017)., T. Yoshikawa *et al.*, Phys. Rev. B **100**, 165311 (2019).
4. T. Okuda *et al.,* Rev. Sci. Instrum. **82**, 103302 (2011).
5. L. Fu, Phys. Rev. Lett. **103**, 266801 (2009)., S. Souma *et al.*, Phys. Rev. Lett. **106**, 216803 (2011).

Time-Resolved Vacuum-Ultraviolet Circular Dichroism for Observing the Membrane Interaction Processes of β-Lactoglobulin

Satoshi Hashimoto[a] and Koichi Matsuo[a,b]

*[a]Graduate School of Advanced Science and Engineering, Hiroshima University,
1-3-1 Kagamiyama, Higashi-Hiroshima, Hiroshima 739-8526, Japan*
*[b] Research Institute for Synchrotron Radiation Science, Hiroshima University, 2-313 Kagamiyama,
Higashi-Hiroshima 739-0046, Japan*

Keywords: Circular dichroism, β-Lactoglobulin, Membrane interaction, Secondary structures, Time-resolved measurement

The structural alteration of water-soluble proteins due to the interaction with bio-membranes (or lipid bilayers) is a starting point for manifesting various biological functions and diseases such as the membrane permeation of protein toxins, formation of amyloid fibrils on membranes, stabilization of the myelin sheath around neuron[1], and drug transportation into the membranes[2]. In this study, to obtain the time-resolved circular-dichroism spectra of protein in the process of membrane interaction, we have developed a TR microfluidic mixing device dedicated in the dynamic observation of protein structures under the membrane interaction (Figure 1) and installed the TR system into the vacuum-ultraviolet circular dichroism (VUVCD) instrument using a synchrotron radiation. The system was also applied to analyze the kinetic parameters and the formation of intermediates in the membrane interaction processes (from native- to membrane-bound-states) of β-lactoglobulin (bLG). [3]

The CD spectra of bLG in various lipid/protein (L/P) concentration ratios (L/P=0~100) showed that bLG transformed from β- to α-rich conformations due to the membrane interaction with the two-state transition and it completely formed the M-state at L/P=50 (Figure 2). The TR-CD spectra after mixing bLG and lysoDMPG micelle solutions were measured in the wavelength range of 180-260 nm within 1-60s (Figure 3). In this interaction process, bLG had the β-α conformation change with more than two transition states. To obtain the rate constants for the interaction, global fitting analysis with biexponential functions were conducted for all TR-CD spectra dataset and two different rate constants were determined, indicating the presence of one intermediate state (I-state). Further, the CD spectrum of the I-state was extracted by considering the two rate constants. From the analyses of secondary structures in the M- and I-states, we discussed on the α-helical regions of bLG that interacted with membrane and disclosed that the native → I and I → M transitions were attributed mainly to electrostatic and hydrophobic interactions, respectively. TR-VUVCD system would be useful technique for characterizing the interaction mechanism between protein and membrane.
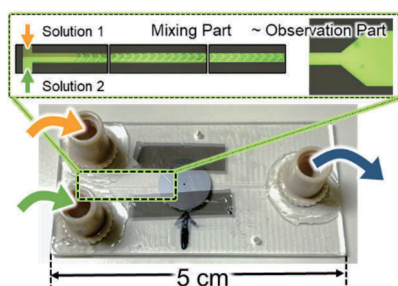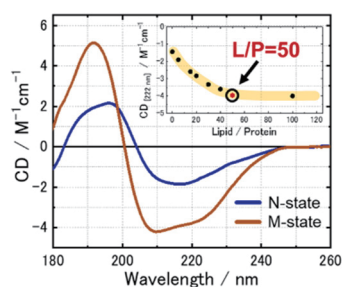

Figure.1 TR cell
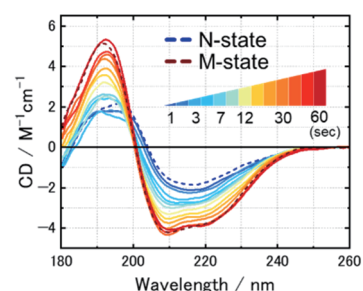

Figure.2 The CD spectra of bLG

Figure.3 TR-CD dataset

REFERENCES

1.   M. Kumashiro, Y. Izumi, and K. Matsuo, *Proteins*, **89**, 1251–1261 (2021).
2.   K. Matsuo and K. Gekko, *Biochemistry*, **48**, 9103–9111 (2009).
3.   S. Hashimoto and K. Matsuo, Anal. Chem., **96**, 10524-10533 (2024).

Spectroscopic and theoretical characterization of the salt effect on the interaction between α-Synuclein and membrane

Ryota Imaura[a], Koichi Matsuo[b]

[a]Graduate School of Advanced Science and Engineering, Hiroshima University
[b]Hiroshima Synchrotron Radiation Center, Hiroshima University,

Keywords: Synchrotron radiation circular dichroism; MD simulation; α-Synuclein; Membrane; Protein-membrane interaction; Secondary structures.

One of the amyloidosis associated with neurodegenerative disorders is Parkinson's disease (PD), which is caused by the formation of amyloid fibrillar aggregates or Lewy bodies in neuron, and these fibril formations are known to be attributed by the interaction of α-synuclein (αS) with the synaptic vesicle membranes [1]. αS is composed of 140 amino acid residues and is divided into three regions: N-terminal region (residues 1-60), non-amyloid β-component (NAC) region (residues 61-95), and C-terminal region (residues 96-140) [2]. The salts such as NaCl and $CaCl_2$, which are universally present in cells, were important factors to regulate the characteristics of amyloid fibrils of αS because these salts directly affected the electrostatic interactions between αSs and between αS and membrane, giving some perturbations to the hydrophobic interactions between αS and membrane. Hence the observation of the salt effects including the types and the concentrations are widely studied to characterize the membrane interaction mechanism and the fibril formation mechanism of αS. In this study, synchrotron radiation techniques, vacuum-ultraviolet circular dichroism (VUVCD) [3] and linear dichroism (LD) spectroscopy, were used to characterize the structures of αS on the membrane in the presence or absence of salt (NaCl). Based on these experimental results, the molecular dynamics (MD) simulations were conducted to characterize the salt effect on the interaction between αS and membrane at the secondary structure and amino-acid residue levels.

Thioflavin-T fluorescence showed that the amyloid fibril formations were highly promoted in the presence of salt. The VUVCD spectra showed that αS changed from a random structure to a helical structure as the molar ratio of lipid to protein increased with or without salt. However, the presence of salt largely decreased the helical contents, compared with the case of absence of salt. The LD spectra showed that some helical segment regions and tyrosine (Tyr) residues interacted with the membrane, orienting parallel to the membrane surface, but the presence of salt largely inhibited these interactions. The N- and C-terminal regions of αS, which include one and three Tyr, respectively, were separately simulated by MD in the membrane and we found that Y39 and Y125 would be involved in the membrane interaction in the absence of salt, but not in the presence of salt. These results suggested that the salt should decrease the membrane interaction regions of αS at the helix structure and Tyr residue levels, which would induce the exposure of αS to the solvent, promoting the intermolecular interactions toward to the amyloid fibril formations.

REFERENCES

1. D. J. Selkoe, *Nature,* vol. 426, pp. 900-904, 2003.
2. Aaron D. Gitler, Brooke J. Bevis, James Shorter, Katherine E. Strathearn, Shusei Hamamichi, Linhui Julie Su, Kim A. Caldwell, Guy A. Caldwell, Jean-Christophe Rochet, J. Michael McCaffery, Charles Barlowe, Susan Lindquist, *Proceedings of the National Academy of Sciences,* vol. 105, no. 1, pp. 145-150, 2008
3. Koichi Matsuo, Kunihiko Gekko, *Methods in Molecular Biology,* vol. 974, pp. 253-279, 2013.5.

VUVCD Measurements of dried proteins and its application to protein-membrane interaction study

Kosuke Hayashi[a], Ryota Imaura[a], and Koichi Matsuo[a,b]

[a]*Graduate School of Advanced Science and Engineering, Hiroshima University*
[b]*Hiroshima Synchrotron Radiation Center, Hiroshima University, Hiroshima University*

Keywords: circular dichroism, G3LEA protein, membrane, spin coat, secondary structure

  Proteins in the dry state are utilized in various fields such as pharmaceuticals and food science. It is known that the structural differences between the liquid and dry states are slight for globular proteins [1], but intrinsically disordered protein undergoes a structural alternation from non-regular to regular structures during the dry process, expressing some unique biological functions. Hence, the elucidation of the relationships between the structural alternation and the function expression is attractive targets. In this study, we measured some globular proteins in the dry state using a vacuum-ultraviolet circular dichroism (VUVCD) spectroscopy, which is the powerful tool for secondary structure analysis of proteins, to discuss the preparations methods of dried proteins. Further, we measured the VUVCD spectra of dried G3LEA protein, which has the structural alternation from disordered structure in liquid state to helical structure in the dry state, expressing a protective function of cell membrane [2].

  Eight types of dried globular proteins with different secondary structures were prepared by a spin coating technique and a vacuum drop casting method. As expected, the spin coating can suppress the surface inhomogeneity of the samples compared the drop casting, depressing the artifact within the CD data due to linear dichroism, which were confirmed by the suppression of rotation and inversion CD dependence of dried samples. Dried G3LEA consisting of 22 residues were prepared by the spin coating technique and we confirmed the structural alternation from random structure in liquid state to α-helix structure in the solid state (Figure 1). The CD spectra of dried G3LEA protein were also measured in the presence of two types of liposomes which are composed of net neutral or negatively-charged phospholipids. As a result, the formation of α-helix structures was clearly observed in negatively-charged lipid liposome but not in neutral one. Furthermore, the formation of α-helix structures was further promoted in the lipid liposome of the gel phase, compared to that of the liquid crystal phase. These results indicated that the surface charge of liposome and its liposome fluidity influenced the structural alternations of dried G3LEA protein.
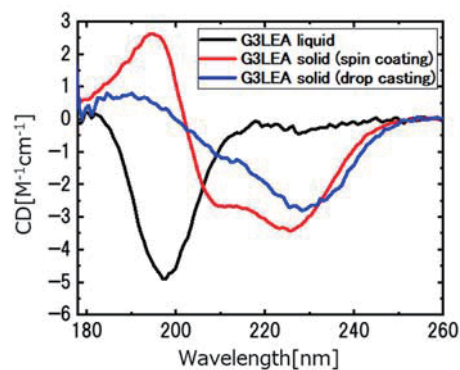

FIGURE 1 VUVCD spectra of G3LEA protein

REFERENCES

1. J.S Yoneda, A. J.Miles, A.P.U. Araujo, and B.A. Wallace, Differential dehydration effects on globular proteins and intrinsically disordered proteins during film formation, *Protein Sci*., **26**, 718-726(2017)
2. T. Furuki, M. Sakurai, Group 3 LEA protein model peptides protect liposomes during desiccation, *Biochim. biophys. acta* **1838**, 2757-2766(2014)

Structural Investigations of Cargo Molecules Inside Icosahedrally Symmetric Encapsulin by VUVCD Spectroscopic Measurements

Shiori Kumamoto[a], Akima Yamamoto[b], Koichi Matsuo[c],

Akifumi Higashiura[b], Daisuke Hira[a]

[a] *Department of Biotechnology and Life Sciences, Sojo University, 4-22-1 Ikeda, Nishi-ku, Kumamoto, 860-0082, Japan.*
[b] *Department of Virology, Graduate School of Biomedical and Health Sciences, Hiroshima University, 1-2-3, Kasumi, Minami-ku, Hiroshima, 734-8551, Japan.*
[c] *Hiroshima Synchrotron Radiation Center, Hiroshima University, 2-313 Kagamiyama, Higashi-Hiroshima, Hiroshima, 739-0046, Japan*

Encapsulins are protein-based organelles found in prokaryotes that compartmentalize specific biochemical functions. These organelles exhibit icosahedral symmetry and can encapsulate various cargo proteins, including ferritin-like proteins, peroxidases, and desulfurases[2]. The encapsulation process is mediated by targeting peptides or encapsulation-mediating domains. Encapsulins have potential applications in bioengineering, vaccine development, and nanoparticle alignment. However, the random orientation of cargo proteins within encapsulins poses a challenge for structural analysis using traditional methods like X-ray crystallography and cryo-electron microscopy (cryo-EM).

The genus *Geobacillus*, part of the *Bacillaceae* family, includes moderately thermophilic bacteria closely related to Bacillus subtilis. *Geobacillus kaustophilus* (*Gk*) has a wide temperature range and excellent growth characteristics, with its genome containing one encapsulin (*Gk*-enc) gene and a cargo protein, iron-mineralizing encapsulin-associated Firmicutes (IMEF). Gk-enc forms 240-mer nanoparticles (FIGURE 1 A). An expression system using the *Gk*-enc gene and IMEF's TP sequence was established to produce stable cargo proteins.

Pyrococcus furiosus (*Pf*) is a hyperthermophilic archaeon living near deep-sea thermal vents. Its encapsulin, a 345 amino acid protein, has a capsid linked to an N-terminal ferritin-like domain. The capsid structure is known, but the NTD structures remain unclear (FIGURE 1 B, C) [3, 4].

Encapsulins from *Geobacillus kaustophilus* (*Gk*) and *Pyrococcus furiosus* (*Pf*) were prepared and purified. The Gk-encapsulin (*GK*-enc) and its cargo protein myoglobin (Mb-TP) were expressed in *E.coli.* and purified using Ni-affinity chromatography. The *Pf*-encapsulin (*Pf*-enc) and its N-terminal domain (*Pf*-enc-NTD) were also expressed in *E. coli* and purified. VUVCD spectra were measured at the Hiroshima University Synchrotron Radiation Center to evaluate the secondary structures of the encapsulins and their cargo proteins.

The VUVCD spectra of *GK*-enc and *GK*-enc-Mb (FIGURE 2 A) revealed that the cargo protein Mb-TP was correctly folded within the encapsulin. The secondary structure analysis showed an increase in helical content for *GK*-enc-Mb compared to empty *GK*-enc. For *Pf*-enc, the VUVCD spectra (FIGURE 2 B, C) indicated that the N-terminal domain (*Pf*-enc-NTD) exhibited a different secondary structure when encapsulated within the full particle compared to its isolated form. This suggests that the structure of *Pf*-enc-NTD is influenced by its encapsulation within the full particle.

The study demonstrates that VUVCD spectroscopy is a valuable tool for evaluating the secondary structures of cargo proteins within encapsulins. The findings indicate that the encapsulation process can

influence the folding and structure of cargo proteins. This structural information is essential for the development of encapsulin-based applications in bioengineering and vaccine development. The approach used in this study could become a standard method for evaluating the internal structures of encapsulins in future research.
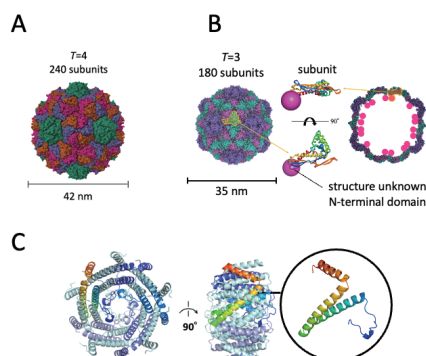

FIGURE 1. Ribbon models of encapsulins (A) 240-mer Encapsulin from *Quasibacillus thermotolerans*, (B) 180-mer Encapsulin from *Pyrococcus furiosus* (*Pf*-enc) (C) *Pf*-enc N-terminal domain (*Pf*-enc-NTD) and the structure within the circle represent the monomer. [1]
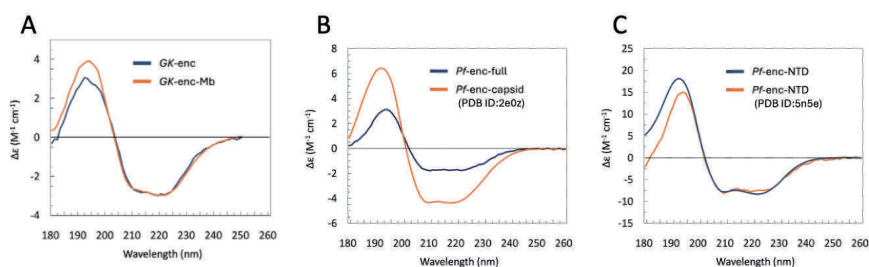
FIGURE 2. (A) CD spectra of *Gk*-enc and *Gk*-enc-Mb, (B) CD spectra of *Pf*-enc-full with simulation spectra of *Pf*-enc-capsid (PDB ID:2e0z) and (C) CD spectra of *Pf*-enc-NTD with simulation spectra of *Pf*-enc-NTD (PDB ID:5n5e). [1]

TABLE 1. Secondary structure contents of *Gk*-enc [1]

	Gk-enc (%)	*Gk*-enc-Mb (%)	Mb-TP (%) (simulation)
Helix	18.8	24.4	60.7
Antiparallel	24.0	22.5	0.2
Parallel	0.8	0	2.1
Turn	14.5	14.9	13.7
Others	41.9	38.2	23.3

TABLE 2. Secondary structure contents of *Gk*-enc [1]

	Pf-enc-full (%)		*Pf*-enc-capsid (%) (from PDB:2e0z)		*Subtraction Pf*-enc-full of *Pf*-enc-capsid (%)		*Pf*-Enc-NTD (%)	
Helix	13.6	(50)[a]	26.9	(63)	8.6	(11)	61.9	(80)
Antiparallel	29.7	(108)	10.0	(24)	44.5	(57)	0	(0)
Parallel	0	(0)	9.1	(21)	0	(0)	0.4	(1)
Turn	15.7	(57)	12.5	(30)	17.4	(22)	0	(0)
Others	41.1	(150)	41.5	(98)	29.6	(38)	37.7	(49)
total	100.0	(365)	100.0	(236)	100.1	(129)	100.0	(129)

[a] Values in parentheses indicate the number of amino acid residues in the secondary structures.

REFERENCES

1. Kumamoto *et al.*, "Structural Investigations of Cargo Molecules Inside Icosahedrally Symmetric Encapsulin by VUVCD Spectroscopic Measurements", *Chirality*, 36: e23700, 2024
2. Giessen TW and Silver PA., "Widespread distribution of encapsulin nanocompartments reveals functional diversity", *Nat Microbiol*, 2: 17029, 2017
3. Akita F *et al.*, "The crystal structure of a virus-like particle from the hyperthermophilic archaeon Pyrococcus furiosus provides insight into the evolution of viruses" *J Mol Biol*, 368: 1469-1483, 2007
4. He D *et al.*, "Conservation of the structural and functional architecture of encapsulated ferritins in bacteria and archaea", *Biochem J*, 476: 975-989, 2019

Monitoring the Self-Assembly of Alginate Hydrogel Using Synchrotron Radiation Circular Dichroism

Tatsuki Haga[a], Masaya Yoshid[a], Takeharu Haino[a], Koichi Matsuo[b] and
Mohamed I.A. Ibrahim[b]

[a]*Graduate School of Advanced Science and Engineering, Hiroshima University.*
[b]*Hiroshima Synchrotron Radiation Center (HiSOR), Hiroshima University, 2-313 Kagamiyama, Higashi-Hiroshima, Hiroshima 739-0046 Japan.*

Keywords: Alginate, Hydrogel, Self-Assembly, CD, AFM

Circular dichroism (CD) spectroscopy, traditionally used for studying the secondary structure of proteins and peptides [1], has not been yet established for studying polysaccharides (PSs). The current study has explored the potential of using CD in structural changes associated with PS hydrogelation. Certain PSs can change from a liquid to a gel when exposed to light, ions, or temperature. Alginate, an ecofriendly and nontoxic PS used in medicine and food, is especially known for forming hydrogels when mixed with polyvalent ions [2]. In the food industry, alginate serves as an additive to enhance texture and shape. This function is closely related to the conformational changes during sol-gel transitions, so structural analysis of alginate is helpful for maximizing its function as an additive.

Herein, CD experiments using synchrotron radiation (SR) light were carried out to investigate the structural changes associated with gel formation in the presence and absence of metal ions. Monovalent ions such as Na^+, K^+, and Li^+ did not induce hydrogel formation, whereas hydrogels were obtained by divalents (e.g., Ca^{2+}, Ba^{2+}, Cu^{2+}, and Zn^{2+}), as well as trivalent ion (e.g., Fe^{3+}). The cations exhibited different influences on the native conformation of alginate, suggesting variations in the assembly of the alginate chains in the presence of different ions. Additionally, discrepancies in CD spectra reflected that the formed hydrogels possessed diverse mechanical, physical properties, and morphology.

The formulation of hydrogels is an evidence of the self-assembly phenomeneon. Alginate chains are inter-connected, forming a cross-linked 3D-network structure that entraps water molecules, leading to hydrogel formation. Hence, to construct the self-assembly/gel phase diagram based on the CD observations, concentration-dependent experiments, varying alginate concentrations or polyvalent ion concnetrations (i.e., Ca^{2+}), were conducted using a CD spectrometer. The concentration of the polyvalent ion that causes no change in the CD spectrum of alginate or that self-assembly of alginate chains was terminated (**Figure 1**, left) was marked as the initiation of aggregation. As a result, a Ca^{2+} concentration of 1.56 mM, at 1.0 mg/ml alginate concentration, was referred to the transition concentration from the self-assembly to aggregation which is followed by hydrogel formation (**Figure 1**, right). This finding was reinforced by atomic force microscopy (AFM) imaging, which showed increased cross-linking and thichness of fibers at higher Ca^{2+} concentration (2.5 mM) (**Figure 2**).
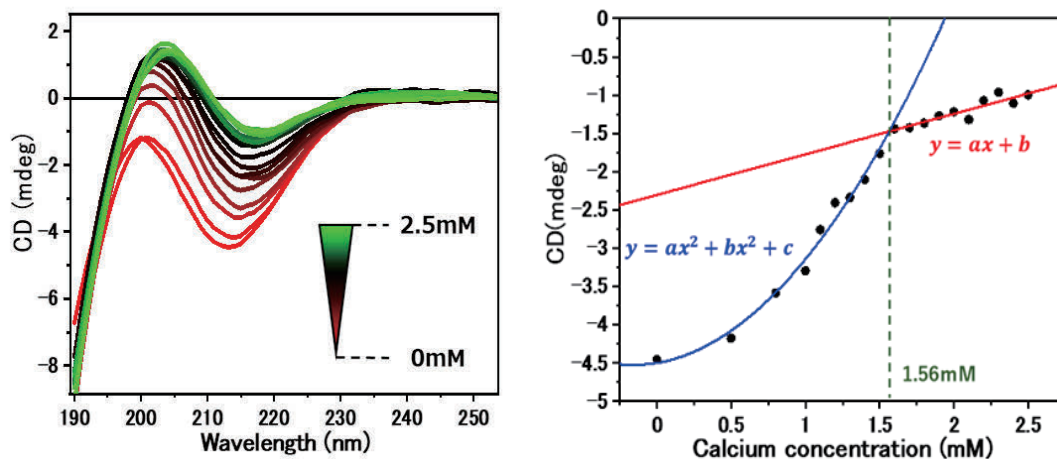
FIGURE 1. CD spectrum of alginate (1.0 mg/ml) as a function of Ca^{2+} concentrations (0.5 mM ~ 2.5 mM) (left), and self-assembly transition diagram based on CD observations (right).
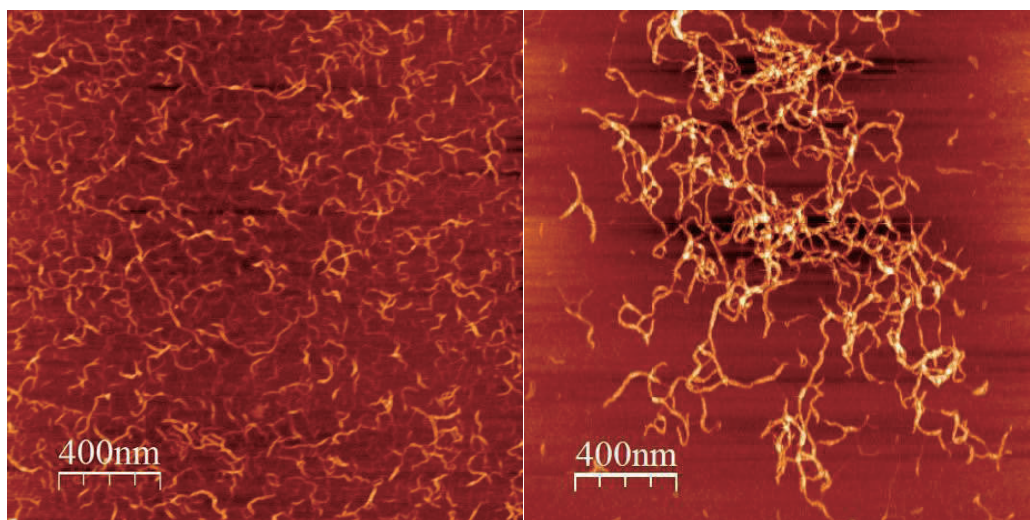

FIGURE 2. AFM images of the alginate-Ca^{2+} system with [alginate] = 1.0 mg/ml and Ca^{2+} concentrations of 1.0 mM (left), or 2.5 mM (right).

Ongoing investigations are underway to further explore the alginate-Ca^{2+} hydrogel system using SRCD, aiming to study the kinetics and thermodynamics of hydrogelation process.

REFERENCES

[1] K. Matsuo, G. Kunihiko, *Bulletin of the Chemical Society of Japan,* 2013, **86**, 675-689.
[2] J. Brus, M. Urbanova, J. Czernek, *Biomacromolecules,* 2017, **18**, 2478–2488.

Effect of Glucose on the Thermal Stability of Lysozyme

Yasuyuki Maki[a], Shunta Usami[a] and Koichi Matuso[b]

[a]Department of Chemistry, Faculty of Science, Kyushu University
744 Motooka, Nishi-ku, Fukuoka, 819-0395
[b]Hiroshima Synchrotron Radiation Center, Hiroshima University,
Higashi-Hiroshima 739-0046, Japan

Keywords: vacuum-ultraviolet circular dichroism, lysozyme, glucose.

Thermal stability of proteins in aqueous solutions is increased by the addition of sugars, which is due to the preferential exclusion of the sugars from the proteins. In this study, we investigated the effect of glucose on the thermal stability of lysozyme, one of typical globular proteins, by using vacuum-ultraviolet circular dichroism (VUVCD) spectroscopy. VUVCD is an effective tool for analyzing structural change of proteins.

Lysozyme from hen egg white (Seikagaku Corp.) and glucose (FUJIFILM Wako Pure Chemical Corp.) were used without further purification. An acetate buffer solution (pH 4.0, 10 mM) with 10 mM NaCl was used as solvent. The concentration of glucose and lysozyme was 20 w/v% and 5 mg/mL, respectively. The protein solutions were centrifuged at 16,000 × g for 15 min to remove the aggregates before the measurements. The measurement of VUVCD spectra was performed using the synchrotron-VUVCD spectrophotometer of Hiroshima Synchrotron Radiation Center (BL-12). The CaF_2 optical cell with 50 μm path length was used and the spectra were measured from 263 to 175 nm at temperatures from 20 $^{\circ}$C to 90 $^{\circ}$C under a nitrogen atmosphere.

The shape of a VUVCD spectrum of lysozyme without glucose measured at 75 $^{\circ}$C was different from that measured at 20 $^{\circ}$C, indicating thermal denaturation of lysozyme at 75 $^{\circ}$C (Figure 1). On the other hand, the shape of a VUVCD spectrum of lysozyme with 20 w/v% glucose measured at 75 $^{\circ}$C was only slightly changed from that measured at 20 $^{\circ}$C (Figure 1). This result demonstrated that glucose stabilized the native structure of lysozyme.
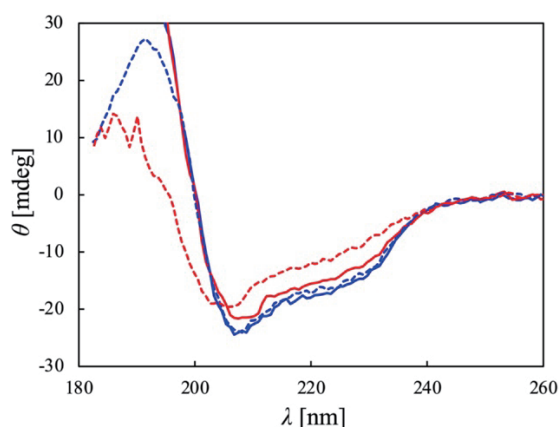

FIGURE 1. VUVCD spectra of lysozyme in 20 w/v% glucose at 20 $^{\circ}$C (blue solid line) and 70 $^{\circ}$C (red solid line), and in acetate buffer at 20 $^{\circ}$C (blue dashed line) and 70 $^{\circ}$C (red dashed line).

Insights into Physical Interactions and Structuration in Self-Assembled Azapeptide Hydrogels Through Spectroscopy Techniques
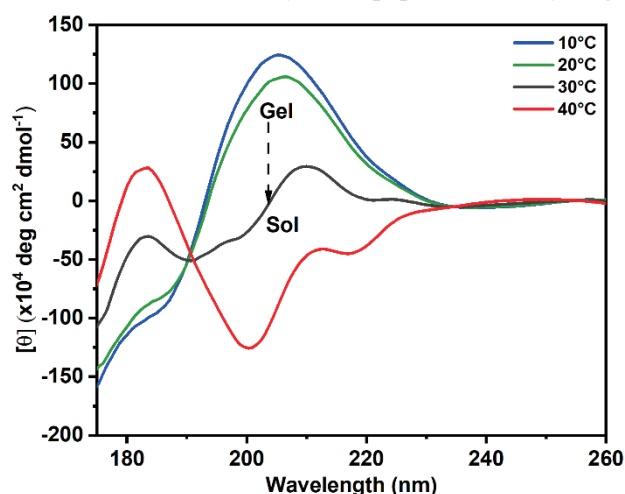
Mohamed Ibrahim[a,b], Jacques Bodiguel[b], Marie-Christine Averlant-Petit[b], and Koichi Matsuo[a]

[a]Hiroshima Synchrotron Radiation Center (HiSOR), Hiroshima University, 2-313 Kagamiyama, Higashi-Hiroshima, Hiroshima 739-0046 Japan.
[b]Université de Lorraine, CNRS, LCPM, F-54000 Nancy France.

Keywords: Self-Assembly, Azapeptides, Hydrogels, Circular Dichroism.

Self-assembly is a captivating phenomenon within supramolecular chemistry, triggering the formation of hydrogels stabilized by non-covalent interactions including hydrogen bonding, π-π stacking, electrostatic interactions, and hydrophobic forces. Supramolecular gels-based low molecular weight molecules find applications in tissue engineering, drug delivery, biosensing, and catalysis [1]. Azapeptides, characterized by their nitrogen atoms, offer unique functionalities and stability, rendering them ideal for the fabrication of supramolecular hydrogels [2, 3]. In this study, two hydrogelator molecules derived from azapeptide family were designed, and structurally elucidated using various spectroscopic techniques. NMR, FTIR, UV-Vis, fluorescence, SEM, and rheology experiments were conducted to explore molecular, supramolecular, mechanical features. In solution, both molecules exhibit monomeric states adopting β-turn conformation stabilized by intramolecular hydrogen bonding, while the supramolecular structure (as revealed by X-ray crystallography) is stabilized mainly through intermolecular hydrogen bonding and π-π stacking (data is not shown). In the gel state, circular dichroism (CD) spectroscopy, is crucial for understanding the secondary structure and self-assembly of azapeptide-based hydrogels [4]. This study sheds light on the conformational changes occurring during the self-assembly process. For example, the temperature dependent experiment revealed the gel-sol transition associated with conformational changes (see **Figure 1**). By integrating principles from supramolecular chemistry, innovative azapeptide design strategies, and sophisticated spectroscopic methodologies, the development of functional hydrogels with tailored properties for diverse applications becomes achievable.

FIGURE 1. Temperature-dependent SRCD spectrum of azapeptide hydrogel (c = 0.8 w/w%, pH = 7.0).

REFERENCES

1. M. J. Webber, E. A. Appel, E. W. Meijer, R. Langer, *Nature Materials*, 2016, **15**, pp. 13–26.
2. F. Rodríguez-Llansola, B. Escuder, J.F. Miravet, *Chemical Society Reviews*, 2015, **44**, pp. 6058–6071.
3. E. R. Draper, M. Wallace, S. Ladame, *Chemical Society Reviews*, 2020, **49**, pp. 7134–7171.
4. N. Berthet, P. Dugourd, R. Antoine, S. Lecomte, *Chirality*, 2019, **31**, pp. 458–476.
5. M. I. A. Ibrahim, G. Pickaert, L. Stefan, B. Jamart-Grégoire, J. Bodiguel, M.-C. Averlant-Petit, *RSC Advances*, 2020,**10**, pp. 43859-43869.

Optical Activity Measurement of Circularly Polarized Lyman-α Light Irradiated and Magnetic Field Applied Amino-acid Films

Jun-ichi Takahashi[a], Masahiro Kobayashi[b], Gen Fujimori[c], Hiroshi Ota[d]
Koichi Matsuo[e], Yoshitaka Taira[d], Masahiro Katoh[d,e], Kensei Kobayashi[c,f]
Yoko Kebukawa[f], Hiroaki Nakamura[b]

[a]Doshisha University, 1-3 Tatara Miyakodani, Kyotanabe 610-0394, Japan
[b]National Institute for Fusion Science, 322-6 Oroshi-cho, Toki 509-5292, Japan
[c]Yokohama National University, 79-5 Tokiwadai, Hodogaya-ku, Yokohama 240-8501, Japan
[d]UVSOR Synchrotron Facility, 38 Nishigo-Naka, Myodaiji, Okazaki 444-8585, Japan
[e]Hiroshima Synchrotron Radiation Center, 2-313 Kagamiyama, Higashi-Hiroshima 739-0046, Japan
[f]Tokyo Institute of Technology, 2-12-1 Ookayama, Meguro-ku, Tokyo 152-8511, Japan

Keywords: Homochirality, Amino Acid, Optical Activity, Circularly Polarized Light, Lyman-α, Circular Dichroism.

The origin of homochirality in terrestrial biomolecules (L-amino acid and D-sugar dominant) remains one of the most mysterious problems in the research for the origins of life. Rational explanations for the chiral asymmetry introduction into biomolecules are required through interdisciplinary collaborations. One of the most attractive hypotheses in the context of astrobiology is cosmogenic scenario; Asymmetric reactions of prebiotic molecules on interstellar dust surfaces in molecular cloud circumstances were introduced by polarized quantum radiation sources in space, that is "chiral radiations" [1, 2].

Among the polarized quantum radiation sources, circularly polarized light (CPL) in the space environment is thought to be one of the most likely causes of the enantiomeric excesses of terrestrial bioorganic molecules. A cosmogenic scenario has attracted attention, which proposes that the radiation fields of CPL induce new optical activity in organic molecules produced in the interstellar environment, leading to the enantiomeric excesses. The radiation fields of CPL are assumed to exist in the scattered light by magnetic field-aligned dust in massive star-forming regions [3] and in synchrotron radiation (SR) or gamma-ray bursts from neutron stars with strong magnetic fields [2]. Ultraviolet light with a wavelength shorter than 230 nm is highly absorbed by bioorganic molecules such as amino acids. Furthermore, this is in the region where the optical response to left- (L-) and right- (R-) CPL is of opposite sign, that is, optical activity is prominent.

To validate the cosmogenic scenario, several ground simulating experiments have been investigated using ultraviolet CPL from high-energy particle accelerators. In this study, we focused on a hydrogen Lyman-α wavelength of 121.6 nm, where strong emission lines are observed in star-forming regions. Furthermore, it is predicted by recent theoretical calculations that the hydrogen Lyman-α light is circularly polarized by the magnetic field-aligned dust scattering in massive star-forming regions. We have carried out irradiation experiments by using circularly polarized hydrogen Lyman-α light to investigate the further photon energy dependence of chiral asymmetric reactions. We formed thin solid film samples of racemic mixture of alanine (DL-alanine) on quartz substrates from crystal powders of DL-alanine by using a thermal-crucible vacuum-evaporation system. The samples were irradiated with L- or R-CPL in hydrogen Lyman-α wavelength of 121.6 nm using the undulator beam line BL1U of UVSOR-III. The irradiated CPL wavelength corresponds to photon absorption bands with the chromophores from the electronic transitions of carboxyl and amino groups (π-σ*) of alanine molecule [4, 5]. The samples were set in a vacuum sample chamber preventing attenuation by air absorption. The 121.6 nm wavelength radiation from the undulator is reflected by a gold-coated mirror located in the mirror chamber directly beam upstream of the sample chamber and then enters the sample chamber. On the beam entrance side of the vacuum sample chamber, a gate valve with an MgF_2 vacuum sealing window (0.5 mm in thickness) was mounted. The use of gold-coated mirror reflections has

made it possible to suppress high-energy higher-order light from the undulator source expecting to reduce the transmittance loss of the MgF_2 window due to high-energy radiation induced defects. The sample substrate was set in the sample holder, in which magnetic field can be applied to perpendicularly to the sample surface (Figure 1). The total photon beam intensity irradiated on the sample was monitored with photoelectron current of a silicon photodiode settled at the beam downstream side of the sample holder.

CD spectra of the CPL irradiated films were measured using the SR-CD beam line BL-12 of HiSOR to clarify the optical activity emergence by CPL irradiation. CD spectroscopy can detect optical activity with a high accuracy because CD spectra sensitively reflects the steric structures of chiral molecules. To delete the effects of linear dichroism components, the CD spectra at sample rotation angles (0, 45, 90, and 135 degrees) from both back and front directions of each were individually measured and averaged them. We already reported the results of the first feasibility study conducted as application proposals to collaborate with UVSOR and HiSOR in FY2022 (6). The measured CD spectra of DL-alanine films irradiated with CPL at 121.6 nm in wavelength indicated the emergence of optical activity depending on the irradiated CPL polarization helicity (L- or R-CPL). In addition, we examined the effect of applying a magnetic field to the sample to investigate the effect of the magnetic field in interstellar space. Comparing with CD spectra of irradiations at 215, 180 and 155 nm in wavelength in our previous study [7, 8], the aspects of the optical activity emergence strongly depend on the irradiated CPL wavelength.

In the experiments for the FY2023 collaborative application proposals, we focused on accumulating reproducibility data of the previous FY2022 results and improving the accuracy of quantification in the quantum efficiency of the emergence of optical activity. Figure 2 shows CD spectra of DL-alanine films after right (R-) and left (L-) circularly polarized Lyman-α (121.6 nm) irradiation with magnetic field (0, ±0.7 T). As shown in this figure, we found a clear emergence of optical activity and a significant magnetic field application effect. The clarification of full mechanism of the optical activity emergence potentially has relevance to the origin of terrestrial bioorganic homochirality stimulated by "chiral photon radiation".
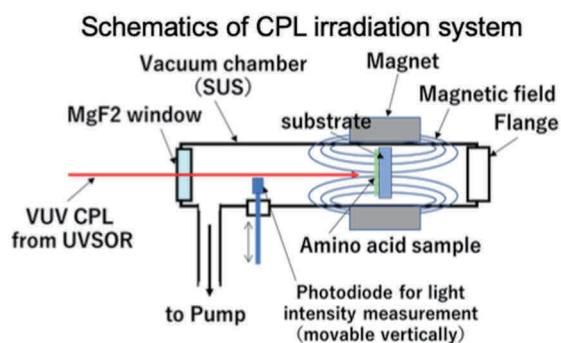
FIGURE 1. Schematic view of circularly polarized Lyman-α (121.6 nm) irradiation system.
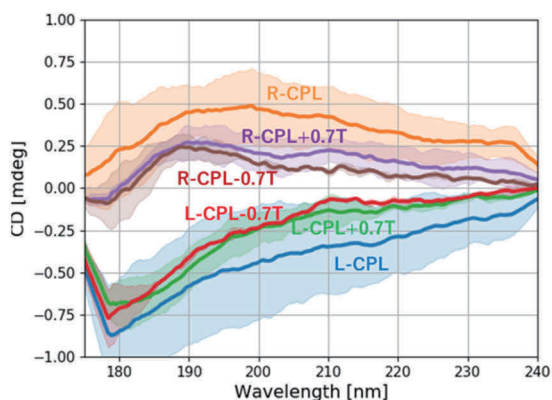

FIGURE 2. CD spectra of on DL-alanine films after right (R-) and left (L-) circularly polarized Lyman-α irradiation with magnetic field (0, ±0.7 T).

REFERENCES

1. W. A. Bonner, *Orig. Life Evol. Biosph.* **21**, 407 (1991).
2. J. Takahashi and K. Kobayashi, *Symmetry* **11**, 919 (2019).
3. H. Fukushima, et al., *Month. Notices Roy. Astron. Soc.* **496** 2762 (2020).
4. M. Tanaka et al., *Enantiomer* **7** 185 (2002).
5. F. Kaneko et al., *J. Phys. Soc. Jpn.* **78** 013001 (2009).
6. M. Kobayashi et al., in Proceedings of A joint ISSOL/IAU-Astrobiology Commission Meeting Origins 2023, Quito, 2023.
7. J. Takahashi et al., *Int. J. Mol. Sci.* **10**, 3044 (2009).
8. J. Takahashi et al., *HISOR Act. Rep. 2019* p.120 (2020).

Soft X-ray Absorption Spectroscopy of Phospholipid Films Supported on Au Substrates by Different Casting Techniques

Yuri Ohura[a], Kakuto Yoshioka[b], Shogo Tendo[b], Akinobu Niozu[a,b], and Shin-ichi Wada[a,b,c]

[a] Faculty of Science, Hiroshima University, Higashi-Hiroshima 739-8526, Japan
[a] Graduate School of Science and Engineering, Hiroshima University, Higashi-Hiroshima 739-8526, Japan
[c] Hiroshima Synchrotron Radiation Center, Hiroshima University, Higashi-Hiroshima 739-0046, Japan

Lipids are one of the major constituents of living organisms. In particular, lipids self-assemble into oriented amphiphilic bilayers, which are the basic structure of the cell membranes. Lipid bilayers not only play an important protective role in maintaining cells, but also serve as sites for information transfer and protein reactions. Therefore, understanding the properties of lipid membranes is fundamental to studying biological mechanisms in detail, and to this end, attempts have been made to reproduce artificial cell membranes by supporting lipids on metal substrates. Lipid membranes supported on solid substrates (Figure 1), such as LB (Langmuir-Blodgett) and vesicle fusion methods, resemble natural cell membranes, and the information obtained are known to be biologically reliable. We have found that even a drop of an organic solution of phospholipid

FIGURE 1. Molecular structure of DPPC phospholipids and schematic bilayer membrane.

molecules onto a gold substrate can form a highly oriented multi lipid-bilayers. In this study, we prepared multi lipid-bilayer membranes by spin-casting method of lipid solutions, aiming to create more uniformly oriented bilayers and to evaluate the state of the bilayers.
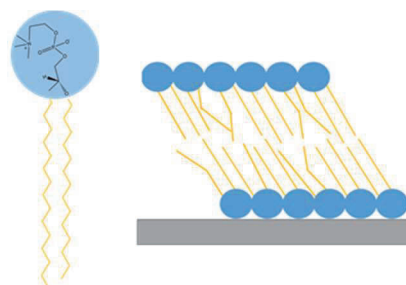
DPPC shown in Figure 1 was used as the phospholipid and dissolved in chloroform to make a lipid solution. The solution was dropped onto Au substrates and dried under a nitrogen stream to create a multi lipid-bilayer membranes. The spin-casting method was also used to create a more uniform bilayer films on the substrates.

The prepared lipid films were characterized by NEXAFS (near edge X-ray absorption fine structure) measurements at HiSOR BL13 and AFM (atomic force microscopy) measurements at the laboratory. NEXAFS spectra were obtained by irradiating soft X-rays in the carbon K-edge region, and the emitted electrons were detected as drain current. The polarization angle dependence of the NEXAFS spectra was measured by changing the incidence angle of horizontally polarized X-rays on the sample surface, and the orientation angle of the organized lipid molecules was thereby determined to evaluate the differences in the multilayer films due to the different preparation methods.

In this study, soft X-ray absorption spectroscopy measurements were performed at different incident angles of soft X-rays to investigate the orientation angles of lipid films prepared by drop and spin-casting methods. Figure 2 shows NEXAFS spectra in the C K-edge region measured at different sample positions for lipid films prepared by drop and the spectrum for the lipid film prepared by spin-casting. The obtained NEXAFS spectra show characteristic resonant excitation peaks at specific energies and different spectral shapes with respect to the incident angle of soft X-ray. In other words, both lipid membranes are highly oriented, despite being multilayered.

Each spectrum can be fitted with a Gaussian function to extract each resonant excitation component. From the area intensities of fitted functions, the orientation angle of the transition dipole moment at each transition was determined. As a result, there is a clear difference between the orientation angles of the lipid films prepared by the drop and spin-casting methods. This is thought to be due to the difference in the method used to prepare the lipid films and the difference in the thickness of the films.

From the Rydberg and σ*(C-C) transitions, the orientation angle of the hydrocarbon chains, which determines the overall shape of the lipid molecules, can be derived specifically. In lipid films prepared by the spin-casting method, the orientation angle is closer to 55 degrees, which is called the "magic angle", than in films prepared by drop-casting. Based on previous studies [1], it is thought that the orientation ordering is reduced in lipid films obtained by spin-casting due to the random structure of some of the hydrocarbon chains. In addition, the NEXAFS spectra of the lipid films obtained by spin-casting are different from those obtained by the drop-casting method in their detailed shape, and are in good agreement with the spectral shape of the single bilayer films in the previous study [1]. These results suggest that the spin-casted lipid films are sufficiently thin to be considered single bilayer films, unlike the drop method, and that the degree of freedom of the molecules constituting the films is increased in this ultra-thin state.

REFERENCES

1. M. Tabuse, A. Niozu, and S. Wada, *HiSOR Activity Report 2021*, 100-101 (2022).
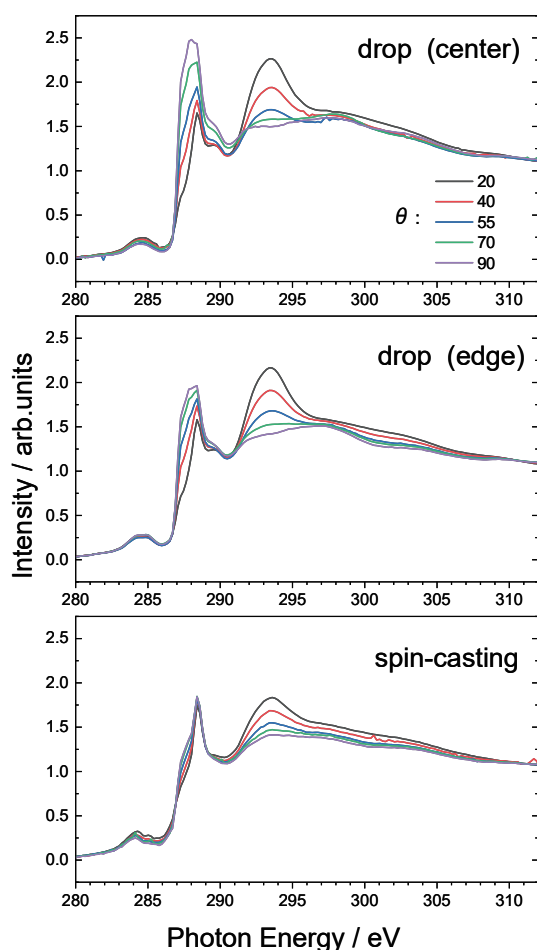
FIGURE 2. Polarization dependent NEXAFS spectra of (upper) center and (middle) edge positions of DPPC drop-casting films and (c) spin-casting film measured at C K-edge. θ: incident angle from the surface, and therefore the angle of electric vector from the surface normal.
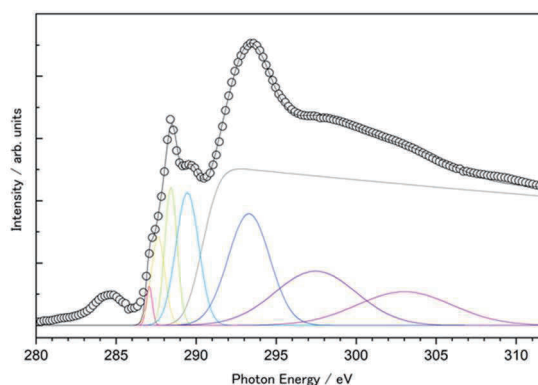

FIGURE 3. Typical result of Gaussian fitting obtained for drop-casting film at 55-degree incidence angle.

Charge Transfer in Gold Substrates and Nanoparticles Coated with Methyl Ester Substituted Aromatic Thiol Molecules

Shogo Tendo[1], Akinobu Niozu[1], Kakuto Yoshioka[1], Jun-ichi Adachi[2], Hirokazu Tanaka[2], and Shin-ichi Wada[1,3]

[1] *Graduate School of Science and Engineering, Hiroshima University, Higashi-Hiroshima 739-8526, Japan*
[2] *Photon Factory, Institute of Materials Structure Science, KEK, Tsukuba 305-0801, Japan*
[3] *Hiroshima Synchrotron Radiation Center, Hiroshima University, Higashi-Hiroshima 739-0046, Japan*

Keywords: Self-assembled monolayers (SAMs), Gold nanoparticles, Site-selective desorption, Core-hole-clock (CHC)

Charge transfer between molecules and metal surfaces is a crucial process with implications for molecular electronics, energy storage, and catalysis. Particularly in nanoparticle films deposited on substrates, where organic molecules coat gold nanoparticles (AuNPs), charge transfer between π-conjugated molecules and metal plays a pivotal role in determining the photoelectric conversion efficiency of dye-sensitized solar cells. In this study, we focused on oligophenyl molecules, which have different molecular lengths, and directly measured the charge transfer time using soft X-rays (Figure 1 (a)–(c)) [1]. Subsequently, we elucidated the electronic properties of the nanoparticle films by comparing the charge transfer dynamics from molecules to flat metal surfaces.

Monophenyl and biphenyl self-assembled monolayers (MP and MBP SAMs, Figure 1 (a), (b)) were prepared on two different metal surfaces. The first SAMs were formed on two-dimensional flat gold substrates (2D SAMs, Figure 1 (d)). The second SAMs were formed on three-dimensional AuNPs, which were drop-cast onto the substrates (3D SAMs, Figure 1 (e)). AuNPs were synthesized by pulsed laser ablation in liquid. The size of the AuNPs was determined to be 7 nm from the surface plasmon resonant peak wavelength, as shown in Figure 2, based on the analytical equation.

Near-edge X-ray absorption fine structure (NEXAFS) spectra and X-ray photoelectron spectra (XPS) were collected at the HiSOR BL-13. The XPS results for the 2D-MP and 3D-MBP SAMs are presented in Figure 3. An important observation from XPS is the similarity in chemical shifts, with no clear discrepancy in the energy position between 2D and 3D SAMs. Any slight variations were attributed to the inhomogeneity of the NP surfaces; nevertheless, the electronic structures of the 2D and 3D SAM remained identical. Figure 4 shows the C and O K-edge NEXAFS spectra. The dominant peaks included π*(C=C) at ~285 eV for the C K-edge and π*(C=O) at 532.0 eV for the O K-edge. Polarization angular
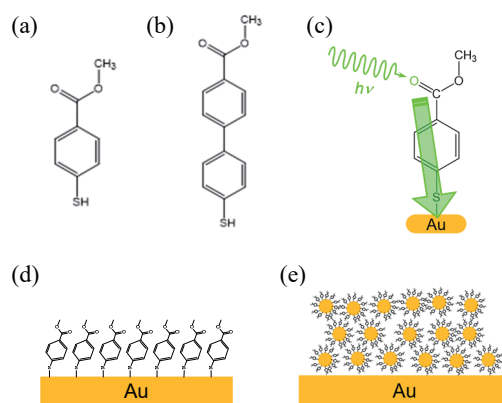

FIGURE 1. Molecular structures of (a) MP and (b) MBP. Images of (c) charge transfer process, and (d) 2D-MP, and (e) 3D-MP SAMs.
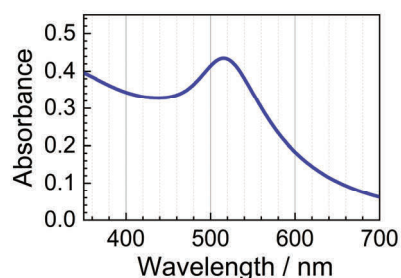

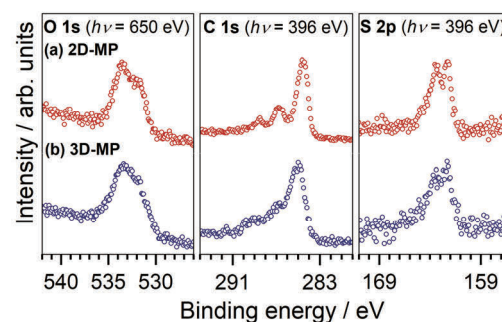**FIGURE 2.** UV-VIS spectrum of AuNP colloids.

FIGURE 3. XPS of 2D-MP and 3D-MP SAMs.

dependence was observed in 2D-MP, and the subsequent fitting analysis suggested that the molecules adsorbed in an upright orientation to the surfaces [2]. In contrast, this phenomenon was not observed in 3D SAMs, likely due to the averaging of the transition dipole moment of molecules on spherical particles. The energy level of the $\pi^*(C=O)$ peaks exceeded the binding energy of the C=O peaks at 531.7 eV in the O 1s XPS spectra, indicating that it was suitable for subsequent resonant Auger electron spectroscopy experiments.

We conducted time-of-flight mass spectrometry (TOF-MS) at Photon Factory BL-2B and utilized the data obtained to construct near-edge X-ray absorption mass spectra (NEXAMS), as shown in Figure 5. The total ion yield (TIY) and partial ion yield (PIY) spectra for both 2D and 3D SAMs exhibited a primary peaks corresponding to $\sigma^*(O–CH_3)$ at 288.9 eV. This observation indicates that 3D SAMs form monolayers similar to those formed by 2D SAMs. The presence of a single sharp peak at 288.9 eV for CH_n^+ (n = 0–3) ions suggests site-selective desorption of CH_n^+ ions from the methoxy group of SAMs [3].

Resonant Auger electron spectra (RAES) were measured at HiSOR BL-13, and the charge transfer times of the 2D and 3D SAMs were determined using the core-hole-clock (CHC) approach. In Figure 6, RAES at O $1s \rightarrow \pi^*(C=O)$ excitation is presented, with peaks corresponding to spectator Auger decay processes observed at ~486 eV and ~511 eV. The RAES at $\pi^*(C=O)$ excitation was fitted with the RAES at post-edge excitation and $\pi^*(C=O)$ excitation of 2D-aliphatic SAMs, which exhibit insulation properties. Using the fitting coefficient and core hole lifetime of O 1s, the charge transfer time for each 2D and 3D SAMs were determined. The charge transfer time of 3D SAMs decreased with increasing chain length, similar to that of 2D SAMs. Furthermore, the charge transfer time between the 2D and 3D SAMs remained unchanged.

Our results suggest that the spectroscopic and electrical properties of 3D SAMs closely resemble those of 2D SAMs. This similarity can be attributed to the fact that the AuNPs synthesized in our study had a diameter of ~7 nm, predominantly comprising {111} terraces on their surfaces [4]. Notably, unique absorption features at the corners and edges of the NPs were not observed in the spectra. In essence, this study serves as a crucial link, extending the applicability of insights into the charge transfer times obtained from diverse molecules observed in 2D to the context of 3D SAMs.

REFERENCES

1. M. Zharnikov, *Acc. Chem. Res.*, **53**, 2975–2984 (2020).
2. J. Stöhr, *NEXAFS Spectroscopy*, Surface Sciences, vol. 25, Berlin, Springer, 1992.
3. S. Wada, H. Kizaki, et al. *J. Phys.: Condens. Matter*, **18**, S1629-S1653 (2006).
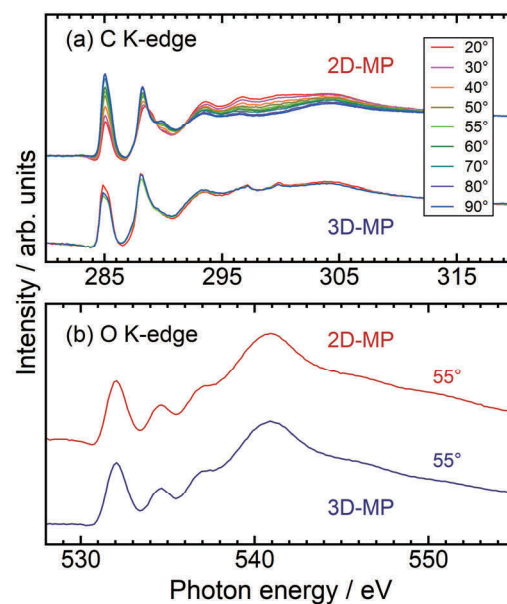4. A. C. Templeton, W. P. Wuelfing and R. W. Murray, *Acc. Chem. Res.*, **33**, 27–36 (2000).

FIGURE 4. (a) Polarization dependence spectra of C K-edge NEXAFS spectra of 2D and 3D-MP. (b) O K-edge NEXAFS spectra of 2D and 3D-MP.
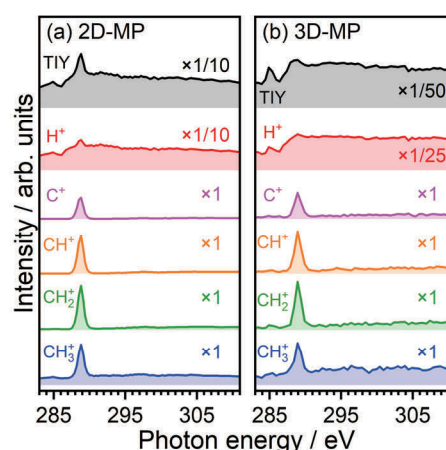

FIGURE 5. C K-edge NEXAMS spectra of (a) 2D-MP and (b) 3D-MP. Total ion yield spectra and partial ion yield spectra of major products.
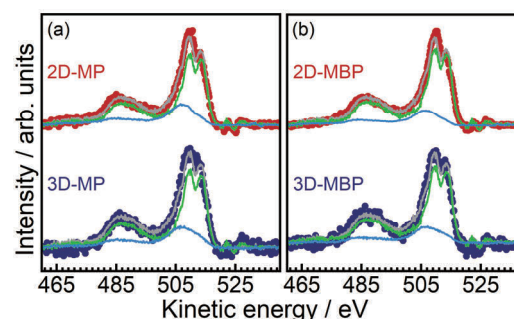

FIGURE 6. RAES of (a) MP and (b) MBP under $\pi^*(C=O)$ excitation after Shirley background subtraction (dotted lines). The reproduced spectra (gray lines) were obtained by fitting with the normal Auger spectra of each MP or MBP SAM (green lines) and the spectator Auger spectra of 2D-aliphatic SAM (light blue lines).

Ultrafast charge transfer through biphenyl and fluorene monolayers studied by core-hole clock spectroscopy

Akinobu Niozu[a], Kakuto Yoshioka[a], Shogo Tendo[a], Shohei Asakura[b],
Yoshikazu Hanaki[b], Jumpei Koizumi[b], Yuri Ohura[b], Junna Yamada[b],
and Shin-ichi Wada[a, c]

*aGraduate School of Science and Engineering, Hiroshima University,
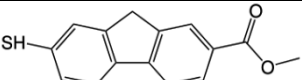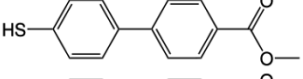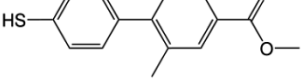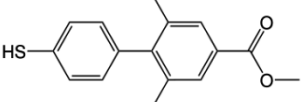Higashi-Hiroshima 739-8526, Japan*
bFaculty of Science, Hiroshima University, Higashi-Hiroshima 739-8526, Japan
*cHiroshima Synchrotron Radiation Center, Hiroshima University,
Higashi-Hiroshima 739-0046, Japan*

Keywords: Self-assembled monolayers, charge transfer, core-hole clock spectroscopy

Nanoscale charge transfer dynamics are crucial for fundamental physical chemistry and applications, such as nanoelectronics and photovoltaics. For these applications, it is crucial to understand the correlation between the molecular structure and charge transport properties. Although molecular conductance has been extensively studied using single-molecule conductance measurements [1], a notable disparity exists between these fundamental investigations of single-molecule junctions and their direct application in functional devices. The use of self-assembled monolayers (SAMs) is a potential solution to bridge this gap given their capacity to form functional devices, thus connecting the insights gained from fundamental studies to practical applications.

TABLE 1.   Molecular structures and torsion angles of the molecules in SAMs.

Name	Structure	Torsion angle / °
MFL		0
MBP		0 [3]
MmBP		52
MdmBP		90

In this study, we investigated ultrafast charge transfer through self-assembled monolayers of biphenyl and fluorene molecules via resonant Auger electron spectroscopy (RAES) using the core-hole clock (CHC) technique [2]. In this approach, molecules are resonantly core-excited with soft X-rays, and the subsequent electron transfer is probed by monitoring Auger decay spectra. The thiolated derivatives of biphenyl and fluorene used in this study are listed in Table 1. The addition of methyl groups induces torsion between the two phenyl rings within the SAMs, resulting in a reduction in π-conjugation. MBP molecules are anticipated to adopt an almost planar conformation [3], similar to that observed in bulk solids. Conversely, the methyl-substituted thiolates (MmBP and MdmBP) are expected to exhibit twisted conformations owing to steric hindrance from the methyl groups. Density functional theory (DFT) calculations of the relaxed molecular geometries yielded torsion angles of 52° and 90° for MmBP and MdmBP molecules, respectively. These molecules have a methyl ester ($COOCH_3$) moiety as the tail group, which serves as the site resonantly excited

with soft X-rays in the CHC experiments.

The methylester-terminated biphenyl and fluorene derivatives were custom-synthesized by and purchased from Tokyo Chemical Industry Co., Ltd. (for MFL, MmBP, and MdmBP) and NARD Institute Ltd. (for MBP). The SAMs were formed by immersing the Au substrates in 1 mM ethanol (for MBP, MmBP, and MdmBP) and toluene (for MFL) solutions of the precursors at 30 °C for 24 h. After immersion, the SAM samples were rinsed with solvent and dried under a flow of N_2 gas. The SAM samples were characterized using near-edge X-ray fine structure (NEXAFS) and X-ray photoelectron spectroscopy (XPS). NEXAFS, XPS, and RAES experiments were conducted at HiSOR BL13. NEXAFS spectra were collected at the C and O K-edges using the total electron yield mode. The XPS and RAES spectra were acquired at an X-ray incidence angle of 45° in the normal emission geometry using Omicron EA125 electron energy analyzer.

The C K-edge NEXAFS spectra showed several peaks corresponding to C 1s→ π^* and C 1s→ σ^* excitations. The polarization dependence of the π^* intensities indicated the orientational order of the molecules within the SAMs. The S 2p XPS spectra of the target SAMs confirmed sulfur species chemisorbed on Au. The NEXAFS and XPS spectra suggest the formation of ordered SAMs on the Au substrates.
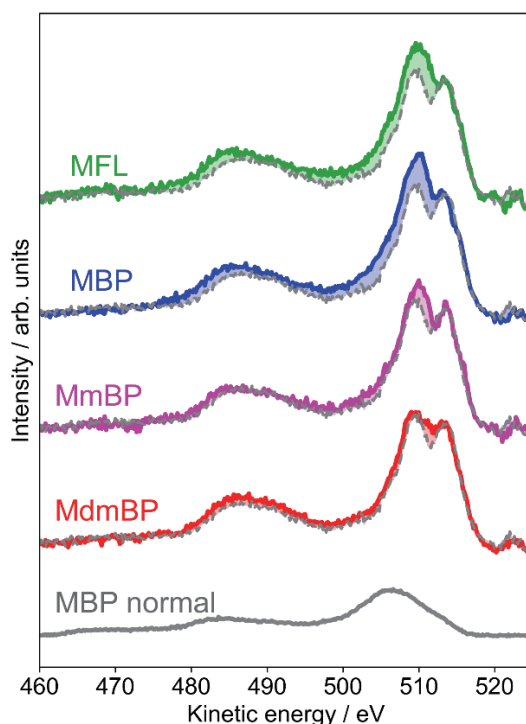

FIGURE 1. RAES spectra of MFL, MBP, MmBP, and MdmBP SAMs. The spectra were compared with the pure resonant spectrum recorded using the MHDA SAM and the normal Auger spectrum of the MBP SAM.

The RAES spectra at the O 1s→ π^*(C=O) excitation are shown in Fig. 1. The spectra were compared with the pure resonant spectrum recorded with an MHDA (HS-$(CH_2)_{15}$-COOCH$_3$) SAM consisting of a long aliphatic chain, which was assumed to show no charge transfer contribution. The spectra for the MFL, MBP, and MmBP SAMs showed an increase in intensity corresponding to normal Auger decay, which indicates ultrafast charge transfer from the molecule to the Au substrate. For a quantitative analysis of the charge transfer dynamics, the RAES spectra were fitted with linear combinations of the normal Auger spectrum and the pure resonant Auger spectrum recorded with the MHDA SAM. The fitting analysis yielded charge transfer times of 16, 16, ~47, and ≳50 fs for the MFL, MBP, MmBP, and MdmBP SAMs, respectively. The CHC results demonstrate the conformational control of ultrafast charge transfer and suggest a negligible influence of the methylene bridge on the charge transfer dynamics.

REFERENCES

1. L. Venkataraman, J. E. Klare, C. Nuckolls, M. S. Hybertsen, and M. L. Steigerwald, *Nature* **442**, 904-907 (2006).
2. M. Zharnikov, *J. Electron Spectros. Relat. Phenomena* **200**, 160-173 (2015).
3. A. Masillamani et al., *Chem. - A Eur. J.* **18**, 10335-10347 (2012).